

# A Multi-Wavelength Study of the Young Star Clusters and Interstellar Medium in the Antennae Galaxies

Qing Zhang<sup>1,2</sup>, S. Michael Fall<sup>1</sup>, Bradley C. Whitmore<sup>1</sup>

## ABSTRACT

We report on a multi-wavelength study of the relationship between young star clusters in the Antennae galaxies (NGC 4038/9) and their interstellar environment, with the goal of understanding the formation and feedback effects of star clusters in merging galaxies. This is possible for the first time because various new observations (from X-rays to radio wavelengths) have become available in the past several years. Quantitative comparisons are made between the positions of the star clusters (broken into three age groups) and the properties of the interstellar medium by calculating the two-point correlation functions. We find that young star clusters are distributed in a clustered fashion, demonstrated by power-law angular auto-correlation functions with slopes in the range  $-0.8$  to  $-1.0$ . The young embedded clusters (ages  $\sim 5$  Myr) are found to be more associated with long-wavelength radiation (mid-infrared and longer), while clusters with ages  $\sim 10$  Myr or older are more associated with short wavelength radiation (e.g., FUV and X-ray). The youngest star clusters are associated with molecular cloud complexes with characteristic radii of about 1 kpc. In addition, there is a weak tendency for them to be found in regions with higher HI velocity dispersions. There is some evidence that both cloud-cloud collisions and shocks from recent star formation can trigger star cluster formation, but no dominant triggering mechanism is identified for the majority of the clusters in the Antennae. Feedback from young bright cluster complexes reveals itself in the form of large H $\alpha$  bubbles and H $\alpha$  velocity gradients in shells around the complexes. We estimate the current star formation rate to be  $\approx 20 M_{\odot} \text{ yr}^{-1}$ , and the gas consumption timescale to be  $\sim 700$  Myr. The latter is comparable to the merging time scale and indicates that star formation has been enhanced by the merger event. Finally, we find that the Schmidt law, with index  $N \approx -1.4$ , is also a good description of the cluster formation triggered by merging in the Antennae. There is some evidence that feedback effects may modify the Schmidt law at scales below 1 kpc.

*Subject headings:* galaxies: individual (NGC 4038/9, the “Antennae” galaxies) — galaxies: interactions — galaxies: star clusters — stars: formation

---

<sup>1</sup>Space Telescope Science Institute, 3700 San Martin Drive, Baltimore, MD 21218, Electronic mail: qzhang@stsci.edu, fall@stsci.edu, whitmore@stsci.edu

<sup>2</sup>Department of Physics and Astronomy, Johns Hopkins University, 3400 N. Charles Street, Baltimore, MD 21218

## 1. Introduction

During the last decade, *Hubble Space Telescope (HST)* observations have revealed the presence of many young star clusters formed in various mergers along the Toomre (1977) sequence (e.g., NGC 4038/9, Whitmore & Schweizer 1995, Whitmore et al. 1999; NGC 3921, Schweizer et al. 1996; NGC 7252, Miller et al. 1997; NGC 3256, Zepf et al. 1999; see Schweizer 1998 and Whitmore 2001 for reviews), as well as a variety of other starburst galaxies (e.g., NGC 1275, Holtzman et al. 1992, Carlson et al. 1998; M82, de Grijs, O’Connell, Gallagher 2001). These young star clusters are often regarded as candidate “young globular clusters”. Indeed, the brightest star clusters formed in mergers have properties (mass, size, etc) similar to those of old globular clusters (GCs). On the other hand, the luminosity and mass functions of the young star clusters are completely different from those of old GCs, being power-laws for the young star clusters (e.g., Whitmore et al. 1999; Zhang & Fall 1999, and references therein), and lognormal or similar centrally-peaked distributions for old GCs (with a “preferred” scale at  $M_V \approx -7.3$  mag and  $M \approx 2 \times 10^5 M_\odot$ , e.g. Harris 1991). Theoretical studies show that disruption by various effects might convert an initial power-law mass function into a centrally-peaked one over a Hubble time (Vesperini 1998; Baumgardt 1998; Fall & Zhang 2000). Thus, the study of young star clusters formed in mergers may increase our understanding of the formation of GCs in the early universe.

Irrespective of the GC issue, the discovery of many young star clusters in mergers provides a good opportunity to observe cluster evolution directly and to test theories that have been proposed for their formation. For example, clusters might form in the cool and compressed gas behind strong shocks resulting from the collision of high speed streams in the violent environment of merging galaxies (Gunn 1980; Kang et al. 1990). It has also been suggested that the turbulent velocities between molecular clouds need to be larger than  $50 - 100 \text{ km s}^{-1}$  before clusters can form, and higher velocity collisions may favor the formation of more massive clusters (Kumai, Basu, & Fujimoto 1993). The high speed motions may also lead to high pressure environments that trigger turbulence or shocks (Jog & Solomon 1992; Elmegreen & Efremov 1997; Elmegreen et al. 2000). Fall & Rees (1985) have proposed a general two-phase structure due to thermal instability and/or shocks that leads to cool clouds compressed by surrounding hot gas (see also Kang et al. 1990). Finally, star formation may be triggered by stellar winds and supernova explosions of young massive stars through compression by turbulent motions (e.g., Larson 1993). We may be able to distinguish between these different models by determining the correlation between young star clusters and factors in their interstellar environment, such as the atomic and molecular gas content, the velocity gradient, and the velocity dispersion.

The Antennae galaxies (NGC 4038/9) provide the nearest opportunity for studying young star clusters formed in a prototypical merger. A large sample of star clusters with a variety of ages has been identified using the WFPC2 onboard the *HST* (Whitmore et al. 1999). Following the original discovery of the young clusters, this merger has been the focus of a full arsenal of state-of-the-art observations across a wide range of wavelength bands over the past few years. These include hydrogen 21 cm line emission (Hibbard et al. 2001), radio continuum at 6 cm and 3.5 cm

with the VLA (Neff & Ulvestad 2000), CO (1-0) observations with the Caltech Millimeter Array (Wilson et al. 2000) and with BIMA (Lo et al. 2000), far-infrared emission at  $450\mu\text{m}$  and  $850\mu\text{m}$  with SCUBA (Haas et al. 2000), at 100-160 $\mu\text{m}$  (Bushouse, Telesco & Werner 1998) and at 60 $\mu\text{m}$  with the Kuiper Airborne Observatory (KAO) (Evans et al. 1997), mid-infrared emission at 15 $\mu\text{m}$  with the ISO (Vigroux et al 1996; Mirabel et al. 1998), and at 10 $\mu\text{m}$  with the NASA Infrared Telescope Facility (Bushouse et al. 1998), H $\alpha$  line and *UBVI* broad-bands with *HST* (Whitmore et al. 1999), far-ultraviolet at  $\sim 1500$  Å with *UIT* (Neff et al. 1997), and soft X-ray observations with *ROSAT* (Fabbiano, Schweizer & Mackie 1997) and with *Chandra* (Fabbiano, Zezas, & Murray 2001). Velocity fields have also been obtained in the hydrogen 21 cm line (Hibbard et al. 2001) and H $\alpha$  line (Amram et al. 1992). The wealth of information available on the Antennae provides a unique opportunity to conduct a comprehensive study of the relation between star clusters and their interstellar environment, and thus provides the ideal laboratory to study how star clusters form. The main limitation in this program is that some observations at longer wavelengths have relatively low spatial resolution (e.g., 17'' at 60 $\mu\text{m}$  and 11.4''  $\times$  7.4'' with hydrogen 21 cm line emission).

In this paper, we explore the spatial distribution of star clusters of different ages and compare these with the intensities observed at other wavelengths. We quantify these comparisons by calculating two-point correlation functions. This objective statistic complements, in a quantitative manner, the subjective impressions one obtains from visually examining the maps. However, we recognize that this technique does not make full use of all the available information. Our goal is to determine the spatial association between star clusters and the properties of their interstellar environment. Some of the questions we hope to explore are: What conditions are required for cluster formation ? Is there direct evidence showing that high speed gas motion and shocks have triggered the formation of young clusters ? How is the cluster formation rate related to local gas content ? Does the Schmidt law hold for star and cluster formation in mergers at sub-galactic scales ?

The plan for the remainder of the paper is the following. In §2, we divide the sample of clusters into three age groups. We describe our method for estimating correlation functions in §3. We then calculate in §4 the autocorrelation functions for star clusters. In § 5 and §6 we cross-correlate the positions of star clusters with intensity and velocity maps. In §7 we discuss the Schmidt laws for star and cluster formation in the Antennae on sub-galactic scales. Finally, in §8 we summarize our results and discuss some implications relevant to the cluster formation scenarios. Throughout, we adopt a distance of 19.2 Mpc for the Antennae ( $H_0 = 75 \text{ km s}^{-1} \text{ Mpc}^{-1}$ ), corresponding to a distance modulus of 31.41.

## 2. Star Cluster Age Groups

The star clusters in the Antennae galaxies are found to have a wide spread of ages, ranging from  $\lesssim 10^6$  years to  $\gtrsim 10^{10}$  years (Whitmore et al. 1999, and tables therein). In this study, we

use the same *HST* WFPC2 data as in Whitmore et al. (1999). From this cluster sample, we form three major age groups of young star clusters: the red clusters (denoted as “R”), the young bright clusters (denoted as “B1”), and the older bright clusters (denoted as “B2”). The R sample contains candidates for the youngest star clusters, since they appear to be still embedded in dusty clouds. The B1 and B2 samples contain more evolved clusters where much of the surrounding gas has been removed. We do not consider intermediate-age ( $\sim 500$  Myr) or old globular clusters because they have small sample sizes and they are likely to have moved far from where they originally formed.

We define the R clusters as clusters with  $V - I > 2$ . To reduce possible stellar contamination we require the extinction-corrected magnitude to be brighter than  $M_V = -10$ . In estimating the extinction for the R sample, we adopt an intrinsic color of  $(V - I)_0 \approx 0.0$ , based on a solar-metallicity cluster less than 3 Myr old in stellar population synthesis models (e.g., Leitherer et al. 1999). Moreover, we exclude individual objects that were identified as foreground stars and old globular clusters by Whitmore et al. (1999).

We verify the young ages of the R clusters by comparing them with stellar population synthesis models in both the  $U - B$  vs.  $B - V$  diagrams and the reddening-free  $Q$ -parameter diagrams, as discussed by Zhang & Fall (1999). We first correct the  $U$ -band magnitudes of the R clusters for the red leak of the F336W filter of the WFPC2 by adopting the values listed in the WFPC2 manual for M stars with values of  $V - I$  similar to those of the R clusters. In Figure 1, we show both the stellar population synthesis models (Starburst99, Leitherer et al. 1999; Bruzual & Charlot 1996, hereafter BC96) and the objects with errors in both  $U - B$  and  $B - V$  smaller than 1 magnitude. We find that 17 out of the 19 objects (nearly 90%) are in the regions of the diagram indicating young ages (i.e.  $Q_1 < -0.7$ ; age  $< 10$  Myr). This confirms the young age of the R clusters. The scatter toward more negative values of  $Q_1$  may indicate that we have not fully corrected for the red leak in the F336W filter. We exclude the objects with  $Q_1 > -0.7$  (corresponding to old ages as discussed above) from the subsequent analysis. This results in a sample of 84 objects, listed in Table 1.

Our R sample includes the well studied cluster #80 from Whitmore & Schweizer (1995), hereafter WS#80, which has age estimates of  $\sim 4$  Myr (Gilbert et al. 2000) and 5.5 Myr (Mengel et al. 2000) from infrared spectroscopy. We estimate the extinction of WS#80 to be  $A_V = 5.7 - 6.2$  using  $V - I$  colors and stellar population synthesis models (Leitherer et al. 1999; BC96). Other estimates of the extinction are  $A_V \sim 9 - 10$  (Gilbert et al. 2000) and  $A_V = 4.3 \pm 0.3$  (Mengel et al. 2000). We note that these young clusters are relatively faint due to higher levels of extinction and are thus subject to larger observational errors than bright clusters. This introduces some uncertainty in the separation of heavily obscured young clusters from red stars, which may not be entirely excluded from the R sample.

We identify the B1 and B2 samples with the use of the  $Q_1 Q_2$  diagram by the same procedure as in Zhang & Fall (1999). By comparing the  $Q$  parameters with stellar population synthesis models, we determine the ages, intrinsic colors, and extinction for the clusters. We use the BC96 models

with a Salpeter IMF and solar metallicity. We also require the extinction-corrected  $M_V$  to be brighter than  $-9$ , because almost all known individual stars are fainter than this limit (Humphreys 1983). The mean extinction,  $A_V$ , varies from  $\sim 1.5$  for the youngest B1 clusters ( $t \lesssim 10$  Myr) to  $\sim 0.3$  for the oldest B2 clusters ( $t \gtrsim 100$  Myr). The masses of the clusters are mostly between  $10^4 M_\odot$  and  $10^6 M_\odot$  (Zhang & Fall 1999). The B1 and B2 samples are defined as the clusters with ages  $3 \lesssim t \lesssim 16$  Myr and  $16 \lesssim t \lesssim 160$  Myr, and contain 1560 and 327 objects, respectively. The division at 16 Myr between the two samples is mainly due to a sharp cusp in the tracks of stellar synthesis models in the  $Q_1 Q_2$ -diagram (see Figure 1 of Zhang & Fall 1999). The brightest objects in the B1 sample are listed in Whitmore et al. (1999). We note that the B1 and B2 clusters are selected according to their intrinsic rather than their apparent colors; this procedure minimizes any selection biases caused by obscuration.

We also identify a sample of candidate young stars for the purpose of comparing their distribution with those of the clusters (see §4). About 4000 candidate young stars are selected based on the criteria that they are relatively faint ( $-6.0 < M_V < -9.0$ ) and are located far from the stellar population synthesis models in the  $Q_1 Q_2$ -diagram. Based on their luminosities, most of these objects are probably individual massive stars younger than  $10^7$  years, although some might be small associations where a single star dominates both in brightness and color.

### 3. Correlation Functions

We will adopt the two-point correlation function to explore the distribution of star clusters and their association with flux maps and velocity fields in other wavelength bands. This quantitative measure of clustering is useful as a complement to the visual impression of the maps. Generally, the 3D two-point correlation function  $\xi(r)$  is defined such that  $\bar{n}[1 + \xi(r)]d^3r$  is the probability of finding a neighbor in a shell element with volume  $d^3r$  at a distance of  $r$  from any object in the sample, and  $\bar{n}$  is the average density of objects (cf. Peebles 1980). In principle, for the 2D discrete distribution of star clusters, the autocorrelation function can be estimated as

$$1 + \xi(r) = \frac{1}{N\bar{n}} \sum_{i=1}^N n_i(r) \quad (1)$$

where  $n_i(r)$  is the number density of objects found in the annulus of radius  $r$  centered on object  $i$ , and  $N$  is the total number of objects (e.g., Martinez 1991). When an annulus extends outside the studied region, a boundary correction is applied by only taking into account the included area using a Monte Carlo algorithm. In the case of associating star clusters with a continuous map (e.g., flux or velocity gradient maps), the cross-correlation function is estimated, as

$$1 + \xi(r) = \frac{1}{N\bar{f}} \sum_{i=1}^N f_i(r). \quad (2)$$

The function  $f_i(r)$  is the average flux in an annulus with radius  $r$  centered on cluster location  $x_i$ , and  $\bar{f}$  is the average flux over the whole region.

The large-scale structure of the Antennae galaxies introduces a complication when calculating the correlation functions for the star clusters. Unlike the classical case of determining the correlation function between galaxies on the sky (e.g., Peebles 1980), where large-scale uniformity of the distribution of galaxies is assumed, the star clusters in the Antennae are located in a galaxy with non-uniform large-scale structure. The simple fact that both the star clusters and the emission from the various wavelength bands are only found within the galaxy introduces a positive correlation, even if there is no other physical connection between the star clusters and their interstellar environment. In the following sections we correct for this effect by subtracting a smoothed flux map from the original map, both normalized by their average density. This is equivalent to the subtraction of  $\xi(r)_s$ , obtained from a smoothed flux map that reflects the large-scale structure of the galaxy, from  $\xi(r)_o$ , obtained from the original map. Hence, the “corrected” correlation function is given by

$$\xi(r)_c = \xi(r)_o - \xi(r)_s. \quad (3)$$

In order to calculate  $\xi(r)_s$ , we adopt a Gaussian filter with a FWHM = 3 kpc ( $\approx 32''$ ), which is large enough so that two clusters cannot communicate within 100 Myr at a signal speed of  $\lesssim 30 \text{ km s}^{-1}$ . This smoothing scale is much larger than the resolution of the observations we use in this study, but is less than a quarter of the scale of the WFPC2 field of view.

To subtract the effects of large-scale galactic structure when calculating the autocorrelation functions for clusters and candidate young stars, we use equation (2) along with the following technique to estimate  $\xi(r)_o$  and  $\xi(r)_s$ . We first map the individual objects onto a  $700 \times 700$  grid, which is the same size as the flux maps. The autocorrelation is then calculated between the positions of the individual objects and the density distribution defined by the grid map. The central object on the grid is always excluded to avoid redundant counting of the objects. Finally, since objects are only located within the field of view of the WFPC2, we mask out other regions of the map when calculating the autocorrelation functions.

We also cross-correlate the cluster positions with maps of velocity gradients and velocity dispersions. Note that the correlation is not made with the velocity itself, which would be meaningless. The velocity gradient at each pixel is calculated by finding the largest spread in the integrated line-of-sight velocities within a rectangular box with the equivalent size and orientation of the observed spatial resolution beam. Regions without velocity information are not considered in the calculation of the velocity gradient, and hence are not included in estimating the correlation functions. In this case, we do not need to subtract the smoothed correlation function, as in equation (3), because the method of deriving gradients already removes the large-scale structure of the galaxy.

Finally, we estimate the statistical uncertainties in the correlation functions. For the auto-correlation functions, we adopt an estimate of uncertainty  $N_p^{-1/2}$ , where  $N_p$  is the number of distinct pairs of objects (cf. Peebles 1980, §48). Although this estimate is strictly valid only for

small  $\xi(r)$ , it may provide an approximate indication of the uncertainties when  $\xi(r)$  is large. For the cross-correlation functions we consider only the statistical uncertainty due to the finite number of clusters,  $N$ . This leads to approximate fractional errors of  $1/\sqrt{N}$  in  $1 + \xi(r)$ . Any errors in the determination of the flux and velocity gradients would increase the uncertainty.

With the autocorrelation and cross-correlation functions computed as above, a random distribution of clusters will result in a flat correlation, with  $\xi(r)_c = 0$ . On the other hand, a peaked  $\xi(r)_c$  at small radii indicates a positive correlation. The width of the central peak represents the spatial scale of association between the clusters and the flux for the various wavelength bands (convolved with the resolution), while the absolute value of  $\xi(r)_c$  is a measure of the concentration of flux surrounding the clusters at a given distance  $r$ , relative to the average over the whole galaxy. From a practical standpoint, it should be noted that the resolution can sometimes dominate the determination of the width and amplitude of the peak.

#### 4. The Spatial Distribution of Star Clusters

We first compare the spatial distributions of the young star clusters and the candidate star samples in Figure 2. We label several interesting regions, major bright knots and the nuclei of NGC 4038 and NGC 4039, for later references. The R clusters mainly reside in the “overlap region” (where the main bodies of NGC 4038 and NGC 4039 are superimposed), as well as the western loop of NGC 4038. The B1 and B2 clusters spread more widely over the Antennae galaxies. We find that they have generally similar spatial distributions, although the B1 sample is slightly more clustered than the B2 sample. The distributions of candidate young stars and young clusters are broadly similar, but at small scales, they are distinctly different.

The autocorrelation functions for the cluster samples and the candidate young stars are shown in Figure 3. The panels from the top to the bottom show  $\xi(r)_o$ ,  $\xi(r)_s$ , and  $\xi(r)_c$ , respectively, as defined by Equation (2). The observed correlation functions decrease approximately as power laws up to a distance of  $\approx 15''$ , corresponding to  $\approx 1.4$  kpc. Beyond this scale, they decrease even more rapidly. The smoothed correlation functions, shown in the middle panel, are essentially flat within  $\approx 10''$ . After the subtraction, the corrected correlation functions shown in the bottom panel remain power-laws within  $\approx 8''$ , corresponding to 0.74 kpc. The power-laws have indices of  $-0.83$ ,  $-1.06$ , and  $-0.89$  for the R, B1, and B2 clusters, and are similar to the value  $-0.7$  for galaxies (Peebles 1980), although the reasons for this are presumably very different. It is interesting to note that the autocorrelation functions for the candidate young stars are flatter (with a power-law index of  $-0.41$ ), implying a weaker correlation. The relatively small sample size for the R clusters is responsible for the noisy behavior in the autocorrelation function; however, it is clear that  $\xi(r)$  for the R clusters largely follows those of the B1 and B2 clusters (especially at small  $r$ ) rather than that of the candidate young stars.

We also checked the distribution of the intermediate-age clusters ( $t \sim 500$  Myr) and old globular

clusters identified by Whitmore et al. (1999). The intermediate-age population is more spread out than the young clusters, with most of the clusters situated along streams apparently associated with the tidal tails and the northwestern loop of NGC 4038. The old GCs are mostly found in the disk of NGC 4039. Neither of these groups show evidence of much clustering, suggesting an effect of dispersal and mixing after several galactic orbits.

The two-point autocorrelation function provides some insight into the physical processes of cluster formation. The clustered distribution of young star clusters probably reflects the self-similar structure of the interstellar medium within the molecular cloud complexes. The radius of  $\approx 1$  kpc, beyond which the correlation functions decline, is comparable to the size of giant molecular cloud complexes in the Antennae (0.8 – 1.8 kpc, Wilson et al. 2000). Since the decline is also seen before the effects of large-scale structure are subtracted, it cannot be an artifact caused by the smoothing. We also note that the bright cluster complexes, such as knots G, M, R, S, T in the northwest and B, C, D, E, and F in the south of the Antennae, as marked in Figure 2, all have sizes of  $\sim 0.5$  kpc (see enlarged images in Figures 6 and 7 of Whitmore et al. 1999), in agreement with the scale set by the autocorrelation functions, especially if we take into account the possible contraction of the cloud complexes during cluster formation.

## 5. Cross-correlations between Star Clusters and their Environment

In this section, we explore the cross-correlation between the star clusters and the flux from the Antennae galaxies in various wavelength bands. By studying these correlations we hope to obtain a comprehensive view of how the physical distribution of the clusters is determined by their interstellar environment and to study how this depends upon the stages of their evolution. In the following, we present the maps in order of decreasing wavelengths.

We first overlay the positions of the three age groups of clusters (the R, B1, and B2 samples) on the contours of various flux maps. The maps presented here have an adopted pixel scale of  $0.1992''$ . If not mentioned otherwise, the contours are plotted on a logarithmic scale. In addition to the direct comparisons from the maps, we quantify the spatial association by calculating the cross-correlation functions between the clusters and the flux in various wavelength bands. We only show the  $\xi(r)_c$ 's, with the effect of large-scale galactic structure removed.

### 5.1. HI Line Emission (21 cm)

The hydrogen 21 cm line emission provides a direct measurement of the properties of atomic hydrogen gas, both its content and kinematics. The most recent high resolution and high sensitivity 21 cm observations of the Antennae galaxies were obtained with the VLA in C+D array configuration, as reported by Hibbard et al. (2001). The data with the resolution of  $11.4'' \times 7.4''$  beam (with the robust parameter set to  $-1$ ) were kindly made available by J. Hibbard prior to

publication. They determine that the total atomic gas content is more than  $4.7 \times 10^9 M_\odot$ , and that about 68% of it is in the tidal tails. Within the central disks, most of the HI gas is located in NGC 4038 and the overlap region. Almost all the star and cluster formation occurs in the disks rather than in the tails (cf. Hibbard et al. 2001; Knierman et al. 2001), which implies that the presence of atomic hydrogen alone is not sufficient to cause star formation.

Figure 4 shows the cross-correlation between the integrated flux of 21 cm line emission and the three age groups of young star clusters. The clusters and HI gas have broadly similar distributions, although most of the clusters lie away from the peaks of HI flux. On the other hand, most of the prominent star formation regions have a nearby reservoir of HI, with an offset ranging from 0.2 to 0.9 kpc. The positive cross-correlation functions in panel *d* indicate that cluster formation is related to atomic gas. The correlation is the strongest for the R clusters and becomes weaker as the clusters age. Note that for the B1 and B2 samples,  $\xi(r)$  is essentially flat at scales within  $10''$ , reflecting the fact that the clusters generally reside off the peaks of atomic gas concentrations.

## 5.2. Radio Continuum Emission (6 cm)

Radio continuum emission can come from either synchrotron radiation from young supernova remnants or thermal radiation from ionized gas in HII regions. An earlier radio continuum observation of the Antennae detected both diffuse emission and thirteen discrete sources (Hummel & van der Hulst 1986). More recent high-resolution radio continuum maps (at 6 cm and 4 cm) were obtained with the VLA in its BnA, CnB, and B configurations and are reported by Neff & Ulvestad (2000). They identified 115 compact radio sources, one third of which are associated with HII regions and the others with supernova remnants. In the following comparisons we adopt the 6 cm radio continuum map that was kindly provided by S. Neff and J. Ulvestad before publication. The map has been cleaned using natural weighting with a full-resolution of  $1.72'' \times 1.52''$  and high sensitivity (RMS is  $10.7 \mu\text{Jy}$ ).

We show in Figure 5 the cross-correlations between radio continuum flux and the three age groups of star clusters. The continuum flux occurs mainly in the overlap region of the galaxies, with several prominent point-like sources. There is also a significant amount of continuum flux from the two nuclei and the western loop of NGC 4038. Several of the R clusters are coincident with the peaks of the radio continuum flux, especially in the overlap region and part of the western loop of NGC 4038. Many B1 clusters are located in regions of high continuum flux in the two galactic nuclei and the western loop. However, some B1 clusters in the northern and eastern star formation regions are not obviously associated with the continuum flux. Only a small fraction of the B2 clusters coincide with the continuum flux, since they are more evolved and their massive stars have already gone supernovae. The different association of star clusters with the radio flux is clearly shown in Figure 5*d*. The cross-correlation is strongest for the R clusters and weakest for the B2 clusters.

We also compare, in Figure 6, the locations of the R clusters with the compact radio sources identified by Neff & Ulvestad (2000) with flux larger than twice the detection limit. Also shown are the 200 brightest B1 clusters, with extinction-corrected  $M_V$  ranging between  $-15.7$  and  $-11.5$ . Both the R clusters and the compact radio sources have significant numbers of objects in the overlap region. However, less than half of the compact radio sources in the overlap region are directly associated with the R clusters. Some are associated with bright clumps of B1 clusters, such as knots B, C, D, E, and F. As suggested by Neff & Ulvestad (2000), some of the radio sources that are not obviously associated with star clusters in our sample may be too deeply embedded in dust to be observed in the optical bands.

### 5.3. CO (1-0) Line Emission (2.6 mm)

CO line emission provides a probe of molecular gas within galaxies since it is related to  $H_2$  column density (Strong et al. 1988; Wilson 1995). In an early study of the Antennae galaxies, Stanford et al. (1990) identified three major concentrations of molecular gas, corresponding to the nuclei of NGC 4038 and NGC 4039 and the overlap region, with a total flux of  $430 \text{ Jy km s}^{-1}$ . Recent high resolution observations have detected a more extended distribution of CO in the whole overlap region and in the western loop of NGC 4038 (Lo et al. 2000; Wilson et al. 2000; Gao et al. 2001). With the Caltech Millimeter Array, Wilson et al. (2000) reported  $910 \text{ Jy km s}^{-1}$  of CO flux, corresponding to  $5.3 \times 10^9 M_\odot$ , and Gao et al. (2001) detected a total mass of  $1.5 \times 10^{10} M_\odot$ , both using the CO (1-0) flux to  $H_2$  conversion relation  $N(H_2)/I_{CO} = 3.0 \times 10^{20} \text{ cm}^{-2} (\text{K km s}^{-1})^{-1}$  (Wilson 1995). Note that molecular gas is mainly found in the disks, where the mass of  $H_2$  is  $\sim 10$  times the mass of HI. Five supergiant molecular clouds are identified in the overlap region, with masses in the range  $3 - 6 \times 10^8 M_\odot$  and diameters  $0.8 - 1.8 \text{ kpc}$  (Wilson et al. 2000).

In the following, we mainly use the BIMA observations, which cover the disks of the Antennae galaxies. The map we use is reconstructed from CO contours with known levels (cf. Lo et al. 2000; Plate 6 of Sanders, Surace & Ishida 1999). The spatial resolution is  $6.61'' \times 7.77''$ . We repeated our analysis using the Wilson et al. (2000) CO intensity map and found results similar to those reported below (e.g., the relative ordering of the correlations for the three age groups is the same for  $r < 10''$ ). We prefer the BIMA map since it covers a larger fraction of the Antennae galaxies.

Figure 7 shows the spatial distribution of star clusters (the R, B1, and B2 samples) overlaid on CO (1-0) flux contours. The R clusters show a good correlation with molecular clouds. The overlap region is where most of the molecular gas is detected, and where more than half of the R clusters are located. Many R clusters are clearly projected on the peaks of CO intensity. This is also true in the northeastern arm of NGC 4038. The R clusters that are not obviously associated with CO (1-0) emission are located mainly to the north of the NGC 4038 nucleus. It is not clear if these objects are genuine embedded clusters, due to the possible contamination with stars in the R sample. We note that it is rare to find R clusters near the concentrations of molecular gas in the nuclei. Most B1 clusters, on the other hand, are located near the peaks of CO flux, except for the

young clusters near the nucleus of NGC 4038 (e.g., knots J and K) and knot F on the northeastern side. The B2 clusters, most of which are on the northeastern edge or the western loop of NGC 4038, are associated with relatively weak CO flux.

The cross-correlation functions between the star clusters and molecular gas confirms the above visual impression (Figure 7d). The strongest correlation is for the youngest clusters (the R sample) with a half-maximum of  $\xi(r)$  at  $r \approx 13''$  (1.2 kpc), consistent with the size of molecular clouds measured by Wilson et al. (2000). The coincidence of R clusters with CO flux supports the idea that molecular gas is directly associated with star cluster formation. The correlation is the weakest for the B2 clusters, with a plateau in  $\xi(r)$  at  $r \approx 5.5''$ . One possibility for this plateau is that the molecular gas is being consumed, blown away, or dissociated upon the formation of star clusters (e.g., the eastern star formation region, see §5.9). It is also possible that the molecular clouds migrate differently from the clusters within the galaxy. A velocity difference of  $\sim 5 \text{ km s}^{-1}$  would result in a separation of  $\sim 500 \text{ pc}$  (corresponding to  $5.4''$ ) within 100 Myr. Hence, this plateau in  $\xi(r)$  for the B2 sample can possibly result from the drifting of the clusters.

#### 5.4. Far-Infrared Emission (60 $\mu\text{m}$ )

Far-infrared emission is thought to originate mainly from dust grains mildly heated either by UV photons from massive stars or by interstellar shocks. Emission at 60 $\mu\text{m}$  is found to correlate tightly with the radio continuum for a wide variety of galaxies (Knapp 1990), suggesting massive star formation as the dominant underlying physical cause (Binney & Merrifield 1998). Thus, far-infrared observations should be a valuable tool for revealing the physics of star cluster formation in the Antennae, a prominent starburst containing a large amount of dust.

The Antennae galaxies were observed at 60 $\mu\text{m}$  with the 90 cm Kuiper Airborne Observatory (KAO) with a resolution of 17'', corresponding to 1.58 kpc, as reported by Evans, Harper, & Helou (1997). Half of the total detected flux, 48.7 Jy, is from the overlap region and a quarter from the NGC 4038 nucleus. This is a situation similar to the radio continuum emission, CO (1-0) line emission, and mid-infrared emission (see §5.5). The Antennae were also observed at longer wavelengths (SCUBA 450 $\mu\text{m}$  and 850 $\mu\text{m}$ ), and both warm ( $\approx 30 \text{ K}$ , typical for starbursts) and cool dust ( $\lesssim 20 \text{ K}$ , typical for quiescent galaxies) were found in the overlap region and in the nucleus of NGC 4038 (Haas et al. 2000). In the following we use the KAO 60 $\mu\text{m}$  image, which was kindly made available by R. Evans.

Figure 8 shows the spatial distribution of the R, B1 and B2 samples overlaid on the contours of the 60 $\mu\text{m}$  flux. The R clusters show a good correlation with the 60 $\mu\text{m}$  flux, while the B1 and B2 clusters match the far-infrared flux in many locations, except for the eastern star formation region. This is a location with weak H $\alpha$  emission (see §5.7) and both atomic and molecular gas almost depleted, as seen in Figures 4 and 7. The cross-correlation functions in Figure 8d clearly show the positive association between the age of the star clusters and far-infrared emission. The strongest

correlation is found for the R clusters. This is consistent with our interpretation that most of the R clusters are young embedded objects (see Figure 1 and the discussion in §2), where emission from dust would be expected. While this correlation may partly be due to a selection effect, since dust is responsible for both the red colors of the clusters and the  $60\mu\text{m}$  emission, we note that the B1 and B2 clusters were chosen on the basis of their reddening-free Q parameters (i.e., they can be red or blue) and, hence, do not suffer from this selection effect. In addition, the fact that the B1 sample shows stronger correlation than the B2 sample (by  $2\sigma$ ) provides further support for an age dependence for the dust emission.

### 5.5. Mid-Infrared Emission ( $15\mu\text{m}$ )

Compared with far-infrared emission, mid-infrared emission is thought to be associated with warmer dust grains heated by newly formed massive stars. Its close association with very young stars makes it an excellent probe for formation activity, especially when dust obscuration is significant and objects are invisible in optical bands.

Observations of the Antennae in the mid-infrared ( $12 - 17\mu\text{m}$ ) were obtained with ISOCAM on the Infrared Space Observatory (ISO) with a resolution of  $4.5''$ , as reported by Vigroux et al. (1996) and Mirabel et al. (1998). Half of the detected mid-infrared flux is from the dusty overlap region while the other half is from the two galactic nuclei and the western loop of NGC 4038. There is little  $15\mu\text{m}$  flux in the northeastern extension. Overall, the distribution of mid-infrared flux in the Antennae largely resembles the radio continuum, CO, and far-infrared maps. In the following, we correlate the positions of the star clusters with the ISO mid-infrared digital image kindly provided by I. F. Mirabel and his colleagues.

Figure 9 shows the spatial distribution of the R, B1, and B2 samples overlaid on the contours of mid-infrared flux. The R clusters are largely coincident with the peaks of mid-infrared flux in the overlap region. A good example is WS#80, which coincides with the most luminous infrared source on the ISO map. The B1 clusters are also well correlated with mid-infrared emission. The exceptions are the clumps of clusters located in the eastern star formation region (discussed in §5.4) and south of the nucleus of NGC 4039. The correlation for the B2 clusters is weaker, in that relatively few objects reside in the overlap region where mid-infrared flux is strong.

Figure 9d shows the cross-correlation between the clusters and mid-infrared flux. Evidently, the R and B1 clusters are closely associated with the  $15\mu\text{m}$  emission. In particular, we note that for the first time the B1 sample shows a stronger peak than the R sample. The relatively strong correlation with mid-infrared emission for young clusters (the R and B1 samples) over the relatively weak correlation for older ones (the B2 sample) indicates that dust grains are either heated or formed along with massive star clusters, and either cool or are expelled as the clusters age. The selection effect discussed in §5.4 is again relevant for  $15\mu\text{m}$  emission, but here we are on firmer ground since the difference between the B1 and B2 samples are quite dramatic.

### 5.6. I-band Emission (0.8 $\mu$ m)

So far we have presented the correlations between clusters and long-wavelength radiation related to their gas and dust environment. We now compare the clusters with the distribution of old stars in the host galaxies. These populations are best depicted by the near-infrared bands because of the existence of red giants and the absence of hot blue stars.

The Antennae have been observed in both the J (1.25 $\mu$ m) band (Bushouse & Werner 1990) and K (2.2 $\mu$ m) band (Evans et al. 1997). These images clearly reveal the prominent nuclei and disks of NGC 4038 and NGC 4039. The disks are largely symmetric, except for some bright HII regions adorning the overlap region between the two nuclei and the western loop of NGC 4038, and an extension of the NGC 4038 disk in the east. In the following, we use the I-band image of the Antennae obtained with the F814W broad-band filter of the WFPC2 on *HST* (Whitmore et al. 1999). This image has a resolution of 0.0455" in the PC chip and 0.0996" in the WF chips (corresponding to 4.23 pc and 9.26 pc, respectively), and generally resembles the J and K band images.

We show in Figure 10 the star clusters overlaid on the contours of the I-band flux. The R clusters do not coincide well with the disk or nucleus of either NGC 4038 or NGC 4039, where most of the near-infrared flux is detected. The B1 clusters, on the other hand, spread over the arms of NGC 4038 and NGC 4039 as well as the overlap region. Density enhancements of the B1 clusters coincide with nearly all the I-band point-like sources in the overlap region, the western loop of NGC 4038, and even the extended arm structure of NGC 4039 toward the southeast. The B1 clusters are also found near both nuclei. The situation for the B2 clusters is similar to that of the B1 clusters. As Figure 10d shows, the R clusters and I-band flux have little correlation, contrary to that for the B1 and B2 clusters.

It is possible that obscuration by dust in the overlap region is responsible for the weak correlation between the R clusters and the I-band flux. This is not likely to be the whole story, however, since the J and K images, with much less extinction, look very similar to the I-band image. The second possibility is that the older clusters formed primarily in the disks of NGC 4038 and NGC 4039, alongside existing old stars, while the R clusters are primarily forming in regions of shocked gas at the interface between the two colliding galaxies where there are very few existing old stars.

### 5.7. H $\alpha$ Line Emission (6563 Å)

The H $\alpha$  recombination line is produced in HII regions, either photoionized by hot stars or collisionally ionized by interstellar shocks. H $\alpha$  emission is often treated as an effective indicator of massive star formation. The H $\alpha$  image of the Antennae we analyze here was obtained with WFPC2 using the F658N narrow-band filter (Whitmore et al. 1999) and was continuum subtracted to obtain the flux of pure H $\alpha$  line emission. Both diffuse structures and highly concentrated blobs are traced

by the H $\alpha$  line emission. The bright concentrations of clusters are often surrounded by filaments, which appear to be products of stellar winds or supernovae remnants.

Figure 11 shows the star clusters overlaid on a gray-scale H $\alpha$  image of the Antennae. We do not plot a contour map of H $\alpha$  emission because it is difficult to show the many fine structures within the Antennae. The R clusters follow the overall H $\alpha$  flux distribution, but they are rarely coincident with the strongest H $\alpha$  peaks, either in the western loop of NGC 4038 or in the overlap region, where a large fraction of the H $\alpha$  flux is detected. Instead, they are generally offset from these peaks. This may be because some ionizing UV photons from the R clusters are absorbed by dust rather than by gas. The B1 clusters are associated with nearly all the H $\alpha$  concentrations, demonstrating that H $\alpha$  emission is an excellent indicator of recent cluster formation. The B2 clusters, on the other hand, are not as closely associated with the most prominent H $\alpha$  peaks. This is to be expected since the ionizing radiation from a stellar population decays dramatically after  $\sim 10$  Myr (Leitherer et al. 1999).

An exception to the overall positive correlation between H $\alpha$  concentrations and the B1 clusters is in the eastern star formation region. Here the H $\alpha$  emission is low and there is relatively little absorbing gas or dust. The presence of large number of B2 clusters in this region suggests the possibility that a burst of star formation some 10–100 Myr ago blew away some of the surrounding gas. Some support for this latter speculation is provided by the arc-like shape in the CO (1-0) contours which envelopes the northwestern side of this region (see Figure 7) and the indentation in the west side of the region in the far-infrared map (see Figure 8).

The cross-correlation functions between star clusters and H $\alpha$  line emission is shown in Figure 11d. The correlation for the B1 clusters is much stronger than the correlation for the R clusters or the B2 clusters. Note the very high value of  $\xi(r)$  for the B1 clusters. The half-maximum width of  $\xi(r)$  for the B1 clusters is  $\approx 2.2''$ , which corresponds to  $\approx 200$  pc. This is roughly the distance traveled in 8 Myr at the typical speed of 25 km s $^{-1}$  for stellar winds in the Antennae (Whitmore et al. 1999), and is consistent with the typical size of giant HII regions surrounding the clusters (e.g., knots G, B, K, M, and S; see enlargements in Figures 7 and 8 of Whitmore et al. 1999). Moreover, the dramatic difference in  $\xi(r)$  between the B1 and B2 samples gives us confidence in the selection of different age populations using the reddening-free  $Q$  parameters. Finally,  $\xi(r)$  for the R clusters is low, and has a peak at around 5'' (500 pc), reflecting their off-peak locations away from the bright H $\alpha$  concentrations.

### 5.8. Far-Ultraviolet Emission ( $\sim 1500$ Å)

Far-Ultraviolet (FUV) emission effectively traces young massive O stars while they are hot, provided stellar winds (and possibly supernovae) have blown away the surrounding dust. FUV observations can thus potentially reveal young blue stellar populations at an age of a few million years.

An FUV image of the Antennae was obtained with the Ultraviolet Imaging Telescope (*UIT*) during the Astro-2 mission and reported by Neff et al. (1997). The spatial resolution and pixel spacing of the digital image are  $3''$  (FWHM) and  $1.14''$ , respectively. The total flux of the Antennae in the FUV band is  $\sim 2.9 \times 10^{-13} \text{ ergs s}^{-1} \text{ cm}^{-2} \text{\AA}^{-1}$ . Most of the FUV flux is from NGC 4038 and the eastern edge of the overlap region. Only a small fraction is from the nucleus of NGC 4039. The data we analyze were taken from the *UIT* archive at the STScI.

Figure 12 shows the distribution of star clusters on the *UIT* image. The R clusters show little coincidence with the FUV image, while the B1 clusters match well with almost all the structures, as labeled in Figure 12a. The B2 clusters coincide with some of the major features, such as the eastern star formation region (ref. §5.4) and the western loop of NGC 4038. The co-existence of the B1 and B2 clusters in some of these features suggests a reasonably continuous formation of clusters during the past  $\lesssim 100$  Myr. Moreover, UV flux may linger for as long as 100 Myr after the onset of star formation according to stellar population synthesis models (e.g. Leitherer et al. 1999). While the B1 clusters are clearly sources of FUV emission, the R clusters are too deeply embedded in dust for much of the FUV radiation to escape. These associations are reflected in the cross-correlation functions in Figure 12d, with weak  $\xi(r)$  for the R clusters but strong  $\xi(r)$  for the B1 and B2 clusters. The cross-correlation function for the R clusters has a peak at  $\approx 7''$ , similar to the results for the I-band and H $\alpha$ .

### 5.9. Soft X-ray Emission (0.1 – 2.5 keV)

Soft X-ray emission can originate from several sources: binary stars, supernova remnants (hot gas behind shocks), and the diffuse hot interstellar medium around young stars. It can also result from gas heated by collisional shocks with velocities around  $100 - 200 \text{ km s}^{-1}$ .

X-ray observations of the Antennae were obtained with the *ROSAT* High Resolution Imager (HRI) in 1994 and 1995 and reported by Fabbiano et al. (1997). The HRI energy range is 0.1 – 2.5 keV and the spatial resolution is  $\approx 5''$ . The Antennae show intricate structures in X-rays, including both extended regions and possible filaments where the emission peaks are associated with HII regions. Fabbiano et al. (1997) suggested that most of the observed emission is from a variety of X-ray sources, such as binaries and supernova remnants, and from a diffuse hot ISM. The image we use in the following was processed from Figure 3c of Fabbiano et al. (1997).

Figure 13 shows the distribution of star clusters overlaid on the contours of the *ROSAT* HRI observations. The R clusters have a relatively poor association with the X-ray emission, which is absent in most of the dusty overlap region. This could be due to absorption (mainly by heavy elements). The B1 and B2 clusters, on the other hand, appear to be associated with many of the X-ray features. Fabbiano et al. (1997) reported the coincidence of some radio sources with high X-ray emissivity in the western loop of NGC 4038 and the galactic nuclei. Figure 13d shows the cross-correlation functions for the clusters and X-ray emission. As anticipated,  $\xi(r)$  is large and

almost identical for the B1 and B2 clusters, but is much weaker for the R clusters.

The B1 and B2 clusters are found to be closely associated with X-ray emission in the eastern star formation region where the only other good correlation is with the FUV emission. Young clusters coincide exactly with the point source X-11 (cf. Fabbiano et al. 1997), where radio and infrared emission is weak. This region probably contains clusters with a range of ages. Unlike X-11, its eastern companion X-12 has no associated clusters. As noted by Fabbiano et al. (1997), there is evidence of a super shell surrounding the clusters in the eastern star formation region. As Figure 7 shows, molecular gas surrounds the clusters on the north and west sides of this region. Radio and far-infrared emission also avoid this region, as shown in Figures 5 and 8. A possible explanation is that these clusters, which formed 10 – 100 Myr ago, have experienced supernova explosions, and that their remnants are the source of the X-ray emission. The gas driven to the east by the supernova explosions may have confronted less gas than to the west, hence traveling farther from the clusters.

### 5.10. Robustness of $\xi(r)$

Finally, we discuss how the cross-correlation functions may be affected by excluding unrepresentative regions from the sample. The most prominent example is the eastern star formation region, where there exist more than 100 B1 and B2 clusters but few R clusters. We repeat the calculations of  $\xi(r)$  after excluding this region and then compare with the earlier results. As shown in Figure 14, the difference is generally small or modest (< 25% at small  $r$ ) for the B1 sample, while it is more noticeable for the B2 sample (e.g., for HI, radio continuum, and 60 $\mu$ m). We note that the changes do not alter the relative rank order of the cross-correlation functions for the R, B1, and B2 samples, even in this extreme case.

## 6. Velocity Fields and Star Clusters

Velocity fields in the ISM provide additional information about the formation and evolution of star clusters. On the one hand, the merging of two galaxies involves the global motion of gas, which may have caused shocks and triggered star and cluster formation. On the other hand, feedback (photoionization, stellar winds and supernova explosions, etc.) from newly-formed clusters inputs energy into the ISM and influences the local motions within galaxies. Therefore, velocity fields may contain information concerning both the cause and the effects of the formation of young star clusters.

In the following, we explore the relationship between the clusters and the velocity fields of the HI and HII in the Antennae galaxies. In addition to overlaying the clusters on the velocity maps, we also calculate the cross-correlation function between the star clusters and the velocity gradients and the velocity dispersions. The regions without contours are those with no velocity information

available, and are not considered in the calculation of cross-correlation functions.

### 6.1. HI Velocity Field

The HI (21 cm) mean velocity and velocity dispersion maps we analyze here were obtained with the VLA with a velocity resolution of  $5.21 \text{ km s}^{-1}$  (Hibbard et al. 2001), and are from the same observations as the flux map discussed in §5.1.

Figure 15 shows the clusters overlaid on the contours of the HI intensity-weighted velocity map. Despite the somewhat distorted disk structures, the atomic gas shows a relatively smooth velocity distribution over the two colliding galaxies. High velocity gradients exist in only two regions where the velocity contours are dense. One is located around R.A. =  $12^h 01^m 55.0^s$  and Decl. =  $-18^\circ 52' 00.0''$ , where the overlap region and the base of the NGC 4038 tail are superposed. The other is in the southern part of the overlap region. Overall, the star clusters do not reside preferentially in regions of high or low velocity gradient, as is reflected in Figure 15d.

Figure 16 shows the clusters overlaid on the contours of the intensity-weighted velocity dispersion map. As seen in panel d, there are weak but non-negligible statistical associations for the R ( $2\sigma$ ) and the B1 ( $5\sigma$ ) samples. While none of these correlations are compelling by themselves, the fact that they increase in the age sequence B2, B1, R in a similar way as found in Figures 4, 5, 7, and 8, provides additional support for their reality.

### 6.2. H $\alpha$ Velocity Field

The H $\alpha$  velocity map we analyze was obtained using a Fabry-Perot interferometer on the ESO 3.6m telescope, as reported by Amram et al. (1992). The spatial resolution is  $0.91''$  and the spectral resolution is  $\approx 16 \text{ km s}^{-1}$ . The processed data were kindly provided by M. Marcellin and P. Amram.

Figure 17 shows the clusters with the contours of the H $\alpha$  velocity field superimposed. The H $\alpha$  velocity field in the northern part of NGC 4038 shows a relatively smooth pattern similar to that of the atomic gas, while those in the southern part of NGC 4038 and in the overlap region show many loops and disturbed structures. Interestingly, the three major loops in the overlap region are exactly centered on the knots B, C, and D, as labeled in Figure 17a, with the central line-of-sight velocity smaller than those of the surrounding annuli. The contour loops are indicative of super shells blown by the newly formed star clusters in these regions. We examine knot D in more detail below. Note that similar velocity loops are not seen in other regions, such as knots J, K, G, S, and T, even though these knots also have H $\alpha$  super shells around them (possibly due to the heavy dust obscuration in knots J and K, and the greater ages in knots G, S, and T).

The H $\alpha$  velocity near knot D is  $1457 \text{ km s}^{-1}$ . The velocity gradient is nearly the same on the north, west, and south sides of the knot, with the velocity increasing by  $38 \text{ km s}^{-1}$  at a

distance of  $5.2''$ , corresponding to 0.48 kpc. For comparison, the central velocities of knots B and C are  $1485 \text{ km s}^{-1}$  and  $1442 \text{ km s}^{-1}$ , respectively, and the velocities increase by  $\approx 39 \text{ km s}^{-1}$  and  $\approx 60 \text{ km s}^{-1}$  at distances of 0.5 kpc and 0.28 kpc, respectively. On the fourth (east) side of knot D, a blowout has apparently occurred. As shown in Figure 7, knot D resides near the edge of the molecular cloud complexes in the overlap region. Thus, the eastward opening of the  $\text{H}\alpha$  velocity contours is probably due to the relatively dilute gas in this direction. It is interesting to note that the  $\text{H}\alpha$  velocity contours around knot D exactly match the indentation in the HI flux map in Figure 4, showing the lack of atomic gas to the east. In addition, knots B, C, and D have velocities consistent with their interstellar environment ( $\approx 1500 \text{ km s}^{-1}$ ).

Clearly, there is strong evidence for feedback from the B1 clusters in the overlap region. The outflows from these knots have velocities slightly larger than the typical velocity of  $25 - 30 \text{ km s}^{-1}$  in knots S and K (Whitmore et al. 1999), and may inject a large amount of energy into the local ISM. Moreover, the velocity of the straight dense contours just north of knots C and D increases from  $1495 \text{ km s}^{-1}$  to  $1564 \text{ km s}^{-1}$  within a distance of  $\approx 2.4''$  (0.22 kpc) corresponding to a gradient of about  $314 \text{ km s}^{-1} \text{ kpc}^{-1}$ . We speculate that the outflows in this region may be responsible for triggering the formation of some of the R clusters.

Statistically, there is no obvious correlation between the clusters and the  $\text{H}\alpha$  velocity field for the R and B2 samples in Figure 17d. There is a negative correlation ( $10\sigma$ ) for the B1 sample, due to the flatter velocity gradients in the centers of the super shells than in their surrounding velocity loops. This negative correlation survives the test of regions when measuring the correlation function as long as knots B, C, and D are included.

## 7. The Schmidt Law in the Antennae

The Schmidt law, which relates the star formation rate and the surface density of gas in the form  $\Sigma_{\text{SFR}} = A\Sigma_{\text{gas}}^N$ , has been empirically tested for many galaxies. The index  $N$  is found to be  $1.4 \pm 0.15$  over a large sample including a variety of galaxies from “quiescent” disk galaxies to starbursts (Kennicutt 1998). It is also noted that, for star formation to commence, the density of gas must reach a threshold of  $\sim 10^{20} \text{ H cm}^{-2}$  ( $\sim 1 M_\odot \text{ pc}^{-2}$ ), which appears to be consistent with the critical density of gravitational instability in spiral disks (Kennicutt 1989). Given the prominent star and cluster formation in the Antennae, it would be interesting to check if the Schmidt law is also valid within this pair of merging galaxies.

We explore the relationship between the star formation rate and gas density at various locations within the Antennae galaxies. First we grid the central disk into small regions and calculate the total flux of  $\text{H}\alpha$  as well as the total gas content in each cell by summing up both the atomic and molecular gas. To obtain the mass of the atomic hydrogen from the 21 cm flux we adopt the conversion formula  $M_{\text{HI}}/M_\odot = 2.36 \times 10^5 D^2 \int S_\nu dv$ , where  $D$  is the distance in Mpc and  $S_\nu dv$  is in  $\text{Jy km s}^{-1}$  (Rohlfs & Wilson 2000, their equation 12.57). We obtain a total mass of

$3.95 \times 10^9 M_\odot$  in atomic hydrogen including the tidal tails, consistent with the value reported by Hibbard et al. (2001). To obtain the molecular gas content from the CO (1-0) line emission we use the same conversion factor  $N(\text{H}_2)/I_{\text{CO}} = 3.0 \times 10^{20} \text{ cm}^{-2} (\text{K km s}^{-1})^{-1}$  as in §5.3, and obtain a relation  $M(\text{molecular gas})/M_\odot = 1.60 \times 10^4 (D/\text{Mpc})^2 S_{\text{CO}}/\text{Jy km s}^{-1}$ . This includes an additional correction of 36 % for heavy elements (cf. Rohlfs & Wilson 2000). We thus obtain a total molecular mass of  $1.44 \times 10^{10} M_\odot$  within the central disk of the Antennae, similar to the value reported by Gao et al. (2001). Finally, we convert the flux of H $\alpha$  line emission (continuum-subtracted) into the star formation rate using the relation  $\Sigma_{\text{SFR}}(M_\odot \text{yr}^{-1}) = 7.9 \times 10^{-42} L(\text{H}\alpha)(\text{ergs s}^{-1})$  (Kennicutt 1998; see references therein for the calibration).

Wilson (1995) found that the CO-to-H $_2$  conversion factor varies with the metallicity in the host galaxy. Since NGC 4038 and NGC 4039 have luminosities and morphologies similar to giant spiral galaxies, it is likely that their metallicity is similar to that of the Milky Way and M31. Hence, we will adopt the empirical conversion factor listed above throughout this section. We also note that any variation in the metallicity will shift the data without altering the slope of the  $\Sigma_{\text{SFR}} - \Sigma_{\text{gas}}$  relation. Other factors that may cause variations in the conversion factor include the size of molecular clouds, the temperature of the ISM, and the optical depth of the CO line. Moreover, there may be complications from the dissociation and consumption of molecular gas due to the starburst in the Antennae.

We correct for extinction in the H $\alpha$  flux by assuming a uniform value over the whole galaxy. It is not possible to correct for each individual cluster using the  $QQ$  analysis (see §2), since we only have useful  $U$  measurements (hence  $Q_1$  values) for 37% of the R clusters, where extinction is most important. However, we can correct for each of the three samples using the mean values for the clusters for which we do have  $Q$  values. In this way, we obtain  $\bar{A}_V \approx 4.7$  for the R sample, 1.6 for the B1 sample, and 0.6 for the B2 sample, resulting in an average of  $\bar{A}_V \approx 1.6$  for all clusters. The mean extinction estimated in this way should be regarded as the lower limit since it may be biased toward the least extinguished clusters (i.e., we tend to miss clusters with the highest values of  $A_V$ ). Another method is to estimate the extinction from the measured H $\alpha$ /H $\beta$  line ratio that was reported by Keel et al. (1985). We obtain a value of  $A_V \approx 2.8$  with the intrinsic H $\alpha$ /H $\beta$  ratio of 2.86 (assuming a Galactic extinction law and  $T_e = 10^4$  K, Caplan & Deharveng 1986). Since the line ratio is affected by absorption lines from young stars, this estimate should be regarded as an upper limit. Thus, we find  $A_{\text{H}\alpha}$  to be within the range 1.3 – 2.3, after interpolating between  $A_V$  and  $A_I$ . In the following we will use the middle value of 1.8. Better estimates of extinction can eventually be made as more infrared spectra become available.

The relation between  $\Sigma_{\text{SFR}}$  and  $\Sigma_{\text{gas}}$  in the Antennae galaxies is shown in Figure 18. Figure 18a shows the result from a grid size of  $11.4'' \times 11.4''$  ( $1.06 \times 1.06$  kpc), comparable to the resolution of the HI observations. The data show significant scatter; the Spearman coefficient is 0.72 for the total gas density. Panel b shows the result from a larger grid size of  $28.5'' \times 28.5''$  ( $2.65 \times 2.65$  kpc). The Spearman coefficient is 0.89 for the total gas density. We fit the data by using first  $\Sigma_{\text{SFR}}$  then  $\Sigma_{\text{gas}}$  as the independent variable, and then using the averaged relation as our final result, as shown

by the dotted lines in Figure 18. The slopes of the data in panel *a* and *b* are  $N = 1.20 \pm 0.23$ , and  $1.38 \pm 0.20$ , respectively, and are consistent with the Schmidt law with  $N = 1.4 \pm 0.15$  within the  $1\sigma$  error, especially in the case of the larger grid size. Repeating the analysis using the Wilson et al. (2000) CO intensity map rather than the BIMA map results in correlations with similar slopes. A possible explanation for the poorer relation on smaller grid scales is that below a certain size limit the young clusters may alter their interstellar environment by depleting the local molecular and atomic hydrogen gas. Hence, the Schmidt law may be modified at scales smaller than the range of the feedback effects.

The agreement with the Schmidt law is somewhat surprising, given the large values of  $A_V$  in the overlap region and the fact that we are probably missing some obscured clusters (see §5.2). We have tested the uniformity of this result and the dependence on our simplistic treatment of  $A_V$  by repeating the calculations using only the northern or western half of the maps. Based on the  $QQ$  analysis, the extinction in these regions is much smaller than in the overlap region. The tests show that the slopes for a  $28.5'' \times 28.5''$  grid vary from 1.2 to 1.5, with the slope of 1.4 being always within the  $1\sigma$  uncertainty. The slopes for a smaller grid of  $11.4'' \times 11.4''$  are between 1.0 and 1.1, consistent with the value 1.4 within the  $2\sigma$  uncertainty.

We also present the relationship between the cluster formation rate ( $\Sigma_{\text{CFR}}$ ) and the gas content in the Antennae in Figure 19. The  $\Sigma_{\text{CFR}}$  is defined as the number density of the R and B1 clusters divided by 8 Myr, roughly their average age. The slopes of the fits are  $N = 1.37 \pm 0.51$  and  $N = 1.53 \pm 0.57$  for the upper and lower panels, respectively. The relation between  $\Sigma_{\text{CFR}}$  and gas content has more scatter than that between  $\Sigma_{\text{SFR}}$  and gas content. This might be expected due to small number statistics (e.g., the bottom row of points has  $n = 1$ ), the possibility of missing some embedded clusters due to obscuration, and incompleteness at the faint end. However, the similarity in the slopes of these relations suggests that the Schmidt law is also a valid description of cluster formation in merging galaxies.

We can also estimate how long it would take before all the gas in the Antennae was consumed by star formation at the current SFR (ignoring possible inflow and outflow). This is sometimes called the “Roberts time”,  $\tau_R$ , and is defined as  $M_{\text{gas}}/\text{SFR}$  (cf. Kennicutt, Tamblyn, & Congdon 1994). The overall star formation rate is  $4.0 M_{\odot} \text{ yr}^{-1}$ , derived directly from the total  $\text{H}\alpha$  flux of  $1.13 \times 10^{-11} \text{ ergs s}^{-1} \text{ cm}^{-2}$  within the disk of the Antennae before correction for extinction. The star formation rate is  $21.0 M_{\odot} \text{ yr}^{-1}$  if  $A_{\text{H}\alpha} = 1.8$  is adopted. This is larger than the value of  $5 M_{\odot} \text{ yr}^{-1}$  estimated by Stanford et al. (1990), mainly due to the higher  $\text{H}\alpha$  line flux detected with the *HST*. For comparison, the current star formation rate of the Milky Way is about  $3 M_{\odot} \text{ yr}^{-1}$  (Mezger 1978; Scoville & Good 1989), and that for M82 is about  $2 M_{\odot} \text{ yr}^{-1}$  (e.g., Condon 1992). Taking a total gas mass of  $\approx 1.5 \times 10^{10} M_{\odot}$  in the Antennae, we obtain  $\tau_R \approx 700 \text{ Myr}$ , which is comparable with the merger age of  $\sim 500 \text{ Myr}$  (cf. Mihos, Bothun, & Richstone 1993), but is shorter than the typical Roberts time for spiral galaxies ( $\sim 3 \text{ Gyr}$ , Kennicutt et al. 1994). These time scales indicate that star formation in the Antennae has been enhanced by the merger event.

## 8. Summary

The recent availability of state-of-the-art maps of the Antennae galaxies (NGC 4038/9), covering almost the whole wavelength range from radio to X-ray, has made it possible for the first time to study the relationship between young star clusters and their interstellar environment. The Antennae system provides the ideal laboratory for this study since it is both the youngest and nearest of Toomre's (1977) prototypical mergers. We use these new data to perform a comprehensive study of the correlation between young star clusters of different ages and their interstellar environment in the Antennae.

Using the *UBVI* images from *HST* WFPC2 observations, we identify three age groups of young star clusters in the Antennae: red clusters (the R sample,  $t \sim 5$  Myr), young bright clusters (the B1 sample,  $3 \lesssim t \lesssim 16$  Myr), and older bright clusters (the B2 sample,  $16 \lesssim t \lesssim 160$  Myr). The observations in the other wavelength bands used in this study include 21 cm line emission (HI), radio continuum (6-cm), CO (1-0), far-infrared ( $60\mu\text{m}$ ), mid-infrared ( $15\mu\text{m}$ ), H $\alpha$  line, FUV ( $\sim 1500$  Å), and soft X-ray emissions. Velocity maps are available in 21 cm, CO (1-0), and H $\alpha$  lines. We first calculate the autocorrelation functions for the star clusters, and then study their cross-correlation with the flux maps and the velocity fields. We note that some observations at longer wavelength are restricted to lower resolution (e.g., 1.58 kpc for the far-infrared emission and  $1.06 \times 0.69$  kpc for the HI 21 cm line emission), and thus some important small-scale information is not available. In addition, selection effects caused by isolating the R sample based on color potentially affect the interpretation of some of the correlations (e.g., the  $60\mu\text{m}$  and  $15\mu\text{m}$  observations, which correlate with the presence of dust). This is less of a problem for the B1 and B2 clusters which are selected based on reddening-free  $Q$  parameters rather than their apparent colors.

Our main results are as follows:

1. We find that star clusters form in a clustered distribution. Their two-point autocorrelation function is a power law with index in the range  $-1.0$  to  $-0.8$ . In contrast, the correlation function for the sample of candidate young massive stars is much weaker, with a power-law index  $-0.4$ . Moreover, the scale of  $\sim 1$  kpc, beyond which the power-law correlation functions for the clusters drop dramatically, is consistent with the typical size of giant molecular cloud complexes identified within the Antennae galaxies. These molecular cloud complexes typically have masses of a few times  $10^8 M_\odot$  (Wilson et al. 2000).

2. We find that the cross-correlations between the star clusters and the flux maps vary with wavelength. The R clusters are closely related to long-wavelength radiation, i.e. emission in the 21 cm line, radio continuum, the CO (1-0) line, the far-infrared and mid-infrared. They are poorly correlated with emission that has wavelength shorter than near-infrared, apparently a consequence of obscuration by dust. The B1 and B2 clusters, however, are more closely related to short-wavelength radiation. The B1 clusters are the main sources of the FUV and H $\alpha$  emission, and are associated with many of the X-ray and I-band features. The B2 clusters, while largely following the behavior of the B1 clusters in the correlation with flux in these bands, have ceased to emit many H $\alpha$

photons, but are associated with X-ray and I-band emission. The variation of correlations in the different wavelengths is consistent with the gradual dissociation of clusters from their formation environment: first by heating the dust, then by ionizing the gas, and finally by expelling the surrounding materials through stellar winds and supernova explosions.

3. The tight correlations between the R clusters and the HI 21 cm line and CO (1-0) line emission indicate that gas content, especially molecular gas, is closely associated with cluster formation. Many of the R clusters are spatially coincident with giant molecular cloud complexes in the overlap region and in the western loop of NGC 4038. On the other hand, gas concentrations alone, even molecular, do not guarantee that clusters will form. For example, few R clusters are found in the CO (1-0) flux concentrations and atomic gas just south of the nucleus of NGC 4039, in the southeast extension (see Figure 7), and in the tails, where HI is abundant.

4. There is some evidence for weak correlations between the locations of young star clusters and the velocity dispersion of atomic gas ( $5\sigma$ ). The most prominent ongoing cluster formation in the southern overlap region is coincident with chaotic velocity fields with line-of-sight velocity gradients of  $\sim 100 \text{ km s}^{-1} \text{ kpc}^{-1}$ . This region of high velocity gradient is also the location with the largest velocity dispersion in molecular gas. Wilson et al. (2000) suggested that it is the site where several giant molecular clouds are colliding. Shocks may have triggered the formation of the clusters in this region. However, collisions among molecular clouds do not seem to account for most of the R clusters, which are formed in other, less chaotic locations.

5. There is strong evidence for feedback by young clusters. We find prominent  $\text{H}\alpha$  super shells surrounding bright cluster complexes of the B1 sample, especially in the overlap region. These outflows have typical velocities of  $25 - 30 \text{ km s}^{-1}$  or larger and inject a large amount of energy into the local ISM. They may be responsible for triggering the formation of some of the R clusters (e.g., north of knots C and D where the velocity gradient in ionized gas is large). We thus infer that the Antennae are a complicated system where different triggering mechanisms may be at work.

6. We find that, in the Antennae, the relationship between the star formation rate and the surface density of gas can be described by the Schmidt law with index  $N = 1.4 \pm 0.15$ . The cluster formation rate obeys the same relationship but with more scatter. However, the Schmidt law may be modified at scales smaller than  $\approx 1 \text{ kpc}$ , where feedback effects become important.

7. We estimate the total observed flux of  $\text{H}\alpha$  line emission to be  $1.13 \times 10^{-11} \text{ ergs s}^{-1} \text{ cm}^{-2}$  in the central disk of the Antennae galaxies. The star formation rate is  $\approx 20 M_\odot \text{ yr}^{-1}$ , if  $A_{\text{H}\alpha} = 1.8$  is adopted. This yields a gas consumption time (i.e., the Roberts time) of  $\tau_R \approx 700 \text{ Myr}$ , which is comparable with the merger time but is smaller than that of a typical spiral galaxy, suggesting a major enhancement of star and cluster formation due to the merger event in the Antennae.

We thank John Hibbard for providing the VLA 21 cm intensity and velocity maps and Susan Neff and Jim Ulvestad for the radio (6 cm and 3.5 cm) data prior to publication. We also thank Rhodri Evans for the KAO 60 $\mu\text{m}$  data, Felix Mirabel for the ISOCAM map, Michel Marcellin and

P. Amram for the H $\alpha$  velocity map, and Christine Wilson for the CO (1-0) intensity map. We thank Ron Allen and an anonymous referee for helpful comments that have improved the paper.

## REFERENCES

Amram, P., Marcellin, M., Boulesteix, J., & le Coarer, E. 1992, A&A, 266, 106

Baumgardt, H. 1998, A&A, 330, 480

Binney, J. & Merrifield, M. 1998, Galactic Astronomy (Princeton: Princeton Univ. Press)

Bruzual, A. G., & Charlot, S. 1996, unpublished (BC96)

Bushouse, H. A., Telesco, C. M., & Werner, M. W. 1998, ApJ, 115, 938

Bushouse, H. A., & Werner, M.W. 1990, ApJ, 359, 72

Caplan, J., & Deharveng, L. 1986, A&A, 155, 297

Carlson, M. N., Holtzman, J. A., and the WFPC2 Team 1998, AJ, 115, 1778

Condon, J. J. 1992, ARA&A, 30, 575

Elmegreen, B. G., & Efremov, Y. N. 1997, ApJ, 480, 235

Elmegreen, B. G., Efremov, Y. N., Pudritz, R. E., & Zinnecker, H. 2000, in Protostars and Planets IV, ed. V. Mannings, A. P. Boss, & S. S. Russell (Tucson: Univ. of Arizona Press), 179

Evans, R., Harper, A., & Helou, G. 1997, in Extragalactic Astronomy and the Infrared, ed. G. A. Mamon, T. X. Thuan, & J. T. T. Van (Paris: Editions Frontiers), 143

Fabbiano, G., Schweizer, F., & Mackie, G. 1997, ApJ, 478, 542

Fabbiano, G., Zezas A., & Murray, S. S. 2001, ApJ, 554, 1035

Fall, S. M., & Rees, M. J. 1985, ApJ, 298, 18

Fall, S. M., & Zhang, Q. 2001, ApJ, in press

Gao, Y., Lo, K. Y., Lee, S.-W., & Lee, T.-H. 2001, ApJ, 548, 172

Gilbert, A. M., Graham, J. R., McLean, I. S., et al. 2000, ApJ, 533, L57

de Grijs, R., O'Connell, R. W., & Gallagher, J. S., AJ, 121, 768

Gunn, J. E. 1980, in Globular Clusters, ed. D. Hanes, & B. Madore (Cambridge: Cambridge Univ. Press), 301

Haas, M., Klaas, U., Coulson, I., Thommes, E., & Xu, C. 2000, A&A, 356, L83

Harris, W. E. 1991, ARA&A, 29, 543

Hibbard, J., van der Hulst, J. M., Barnes, J. E., & Rich, R. M. 2001, AJ, in press

Holtzman, J. A., et al. 1992, AJ, 103, 691

Hummel, E. & van der Hulst, J. M. 1986, A&A, 155, 151

Humphreys, R. M. 1983, ApJ, 269, 335

Jog, C. J. & Solomon, P. M. 1992, ApJ, 387, 152

Kang, H., Shapiro, P. R., Fall, S. M., & Rees, M. J. 1990, ApJ, 363, 488

Keel, W. C., Kennicutt, R. C., Hummel, E., & van der Hulst, J. M. 1985, AJ, 90, 708

Kennicutt, R. C. 1989, ApJ, 344, 685

Kennicutt, R. C. 1998, ApJ, 498, 541

Kennicutt, R. C., Tamblyn, P., & Congdon, C. W. 1994, ApJ, 435, 22

Knapp, G.R. 1990, in The Interstellar Medium in Galaxies, ed. H. A. Thronson, & J. M. Shull (Dordrecht: Kluwer), 3

Knierman, K., Gallagher, S. C., Charlton, J. C., et al. 2001, AJ, submitted

Kumai, Y., Basu, B., & Fujimoto, M. 1993, ApJ, 404, 144

Larson, R. B. 1993, in ASP Conf. Proc. 48, The Globular Cluster-Galaxy Connection, ed. G. H. Smith & J. P. Brodie (San Francisco: ASP), 675

Leitherer, C., Schaerer, D., Goldader, J. D., González Delgado, R. M., Robert, C., et al. 1999, ApJS, 123, 3

Lo, K. Y., Hwang, C. Y., Lee, S.-W., Kim, D. C., Wang, W. H., & Lee, T.-H. 2000, in ASP Conf. Ser. 197, XVth IAP Meeting Dynamics of Galaxies: From the Early Universe to the Present, ed. F. Combes, G. A. Mamon, & V. Charmandaris (San Francisco: ASP), 279

Martinez, V. J., 1991, in Lecture Notes in Physics: Applying Fractals in Astronomy, ed. A. Heck & J. M. Perdang, (Berlin Heidelberg: Springer-Verlag), 135

Mengel, S., Lehnert, M. D., Thatte, N., Tacconi-Garman, L. E., & Genzel, R. 2000, ApJ, 550, 280

Mezger, P. G. 1978, A&A, 70, 565

Mihos, J. C., Bothun, G. D., & Richstone, D. O. 1993, ApJ, 418, 82

Miller, B. W., Whitmore, B. C., Schweizer, F., & Fall, S. M. 1997, AJ, 114, 2381

Mirabel, I. F., Vigroux, L., Charmandaris, V., et al. 1998, A&A, 333, L1

Neff, S.G., Hollis, J. E., Hill, J. K., et al. 1997, in Star Formation Near and Far, ed. S. S. Holt & L. G. Mundy (New York: AIP Press), 473

Neff, S.G., & Ulvestad, J. 2000, AJ, 120, 670

Peebles, P. J. E. 1980, The Large Scale Structure of the Universe (Princeton: Princeton Univ. Press)

Rohlfs, K., & Wilson, T. L. 2000, Tools of Radio Astronomy, 3rd ed. (Berlin Heidelberg: Springer-Verlag)

Sanders, D. B., Surace, J. A., & Ishida, C. M. 1999, in Galaxy Interactions at Low and High Redshift, ed. J. E. Barnes & D. B. Sanders (Dordrecht: Kluwer), 289

Schweizer, F. 1998, in Galaxies: Interactions and Induced Star Formation, Saas-Fee Advanced Course 26, ed. D. Friedli, L. Martinet, & D. Pfenniger (Berlin Heidelberg: Springer-Verlag), 105

Schweizer, F., Miller, B., Whitmore, B. C., & Fall, S. M. 1996, AJ, 112, 1839

Scoville, N. Z., & Good, J. C. 1989, ApJ, 339, 149

Stanford, S. A., Sargent, A. I., Sanders, D. B., & Scoville, N. Z. 1990, ApJ, 349, 492

Strong, A. W., Bloemen, J. B. G. M., Dame, T. M., Grenier, I. A., Hermsen, W., et al. 1988, A&A, 207, 1

Toomre, A. 1977, in The Evolution of Galaxies and Stellar Populations, ed. B. M. Tinsley & R. B. Larson (New Haven: Yale Univ. Observatory), 401

Vesperini, E. 1998, MNRAS, 299, 1019

Vigroux, L., et al. 1996, A&A, 315, L93

Whitmore, B. C. 2001, in A Decade of HST Science, ed. M. Livio, K. Noll, & M. Stiavelli, (Cambridge: Cambridge Univ. Press), in press

Whitmore, B. C. & Schweizer, F. 1995, AJ, 109, 960 (WS95)

Whitmore, B.C., Zhang, Q., Leitherer, C., Fall, S. M., Schweizer, F., & Miller, B.W. 1999, AJ, 118, 1551

Wilson, C. D., Scoville, N., Madden, S. C., & Charmandaris, V. 2000, ApJ, 542, 120

Wilson, C. D. 1995, ApJ, 448, L97

Zepf, S. E., Ashman, K. M., English, J., Freeman, K. C., & Sharples, R. M. 1999, AJ, 118, 752  
Zhang, Q., & Fall, S. M. 1999, ApJ, 527, L81

Fig. 1.— Comparison of the R clusters and stellar population synthesis models in the color-color diagram and the reddening-free  $Q$ -parameter diagram. Only the R clusters with errors in  $U - B$  and  $B - V$  less than 1 magnitude are shown. The solid and dotted lines represent the BC96 and Starburst99 models with solar metallicity, respectively. The numbers label the logarithmic age in years for the models. The arrow in the upper panel shows a standard reddening vector with 1 magnitude of extinction. The cross in the lower panel shows the error-weighted average position of the objects with  $Q_1 < -0.7$ . Note that most of the R clusters have an age of  $\sim 5$  Myr.

Fig. 2.— Spatial distribution of the R ( $t \sim 5$  Myr), B1 ( $3 \lesssim t \lesssim 16$  Myr), and B2 ( $16 \lesssim t \lesssim 160$  Myr) clusters and candidate young stars ( $-9 < M_V < -6$ ). The symbols in the right panels are made smaller for clarity. The ellipses label some regions of interest while the letters in panel *b* mark the bright knots of star clusters. The upper and lower crosses (“+”) label the nuclei of NGC 4038 and NGC 4039, at R.A. =  $12^h 01^m 53.0^s$ , Decl. =  $-18^\circ 52' 01.9''$ , and R.A. =  $12^h 01^m 53.5^s$ , Decl. =  $-18^\circ 53' 09.8''$  (J2000.0), respectively, measured from radio continuum (6 cm and 3.5 cm) maps. The straight lines show the WFPC2 window.

Fig. 3.— Two-point autocorrelation functions  $\xi(r)$  of clusters and candidate young stars. The dashed curve is for the R sample, the solid curve is for the B1 sample, and the dot-dashed curve is for the B2 sample. The dotted curve represents the candidate young stars. The vertical lines show the uncertainties in  $\xi(r)$ . The top panel shows the autocorrelation function  $\xi(r)$  without any consideration of the large-scale structure of the galaxy. The middle panel shows  $\xi(r)$  between the objects and their smoothed density distribution (using a Gaussian mask with FWHM = 3 kpc). The bottom panel shows  $\xi(r)$  with the large-scale structure of the galaxy subtracted. Note the flatness in  $\xi(r)_s$  for small  $r$ .

Fig. 4.— Association between 21 cm HI flux (contours) and star clusters (crosses). Panels *a*, *b*, and *c* show the locations of the R clusters ( $t \sim 5$  Myr), B1 clusters ( $3 \lesssim t \lesssim 16$  Myr) and B2 clusters ( $16 \lesssim t \lesssim 160$  Myr), respectively. The HI contour levels are  $4.3, 6.5, 9.7, 14.5, 21.8, 32.7, 49.1, 73.6, 110.5, 165.7 \times 10^{-3}$  mJy km s $^{-1}$ . The ellipse at the lower-right corner of panel *a* shows the beam size of the contour map. Panel *d* shows the cross-correlation functions between the star clusters and HI flux, with the large-scale structure of the galaxy subtracted. The three sets of vertical lines at  $r \approx 1'', 10'', 20''$  show the uncertainties in  $\xi(r)$ . The small vertical tick near the zero point shows the equivalent half width at half maximum (HWHM) of the HI beam. The horizontal axis on the top labels the radius in kpc, assuming a distance of 19.2 Mpc for the Antennae galaxies.

Fig. 5.— Association between radio continuum (6 cm) flux and star clusters. The contour levels are 1.7, 2.6, 3.9, 5.8, 8.8, 13.1, 19.7, 29.5, 44.3, 66.5  $\mu$ Jy. The notations are the same as in Figure 4.

Fig. 6.— Distributions of R clusters, bright B1 clusters, and compact radio sources with flux larger than twice the detection limit identified with radio 6 cm continuum observation by Neff & Ulvestad (2000, their table 3). The size of the open circles approximately represents the resolution of the radio continuum observation. The boxes label the knots B, C, D, E, F, J, and K. The reference point at (0, 0) is R.A. =  $12^h 01^m 52.97^s$  and Decl. =  $-18^\circ 52' 08.29''$  (J2000.0).

Fig. 7.— Association between CO (1-0) flux and star clusters. The contour levels are 2.9, 4.3, 6.5, 9.8, 14.6, 22.0, 33.0, 49.4, 74.1,  $111.2 \times 10^{-3}$  Jy km s $^{-1}$ . The label WS#80 in panel *a* corresponds to the red object #80 listed in Whitmore & Schweizer (1995). The other notations are the same as in Figure 4.

Fig. 8.— Association between far-infrared (60 $\mu$ m) flux and star clusters. The contour levels are 0.8, 1.3, 1.8, 2.3, 2.8, 3.3, 3.8, 4.3, 4.8, 5.3, 5.8, 6.3, 6.8, 7.3, 7.8 ADU (Note: unlike other figures, this is a linear scale). The three sets of vertical lines at  $r \approx 1'', 10'', 20''$  show the uncertainties in  $\xi(r)$ . The notations are the same as in Figure 4.

Fig. 9.— Association between near-infrared (15 $\mu$ m) flux and star clusters. The contour levels are 0.024, 0.037, 0.055, 0.082, 0.12, 0.18, 0.28, 0.42, 0.62, 0.94 mJy. The notations are the same as in Figure 4.

Fig. 10.— Association between I-band flux and star clusters. The contour levels are 0.50, 0.75, 1.13, 1.69, 2.54, 3.81, 5.72, 8.58,  $12.86, 19.30 \times 10^{-18}$  ergs s $^{-1}$  cm $^{-2}$   $\text{\AA}^{-1}$ . The notations are the same as in Figure 4.

Fig. 11.— Association between the H $\alpha$  line flux and star clusters. The H $\alpha$  map is shown in gray scale. The notations are the same as in Figure 4.

Fig. 12.— Association between FUV flux and star clusters. The contour levels are 0.8, 1.2, 1.8, 2.7, 4.0, 6.0, 9.0,  $13.5, 30.4 \times 10^{-18}$  ergs s $^{-1}$  cm $^{-2}$   $\text{\AA}^{-1}$ . The letter labels in panel *a* correspond to the bright cluster regions categorized by Whitmore et al. (1999). The other notations are the same as in Figure 4.

Fig. 13.— Association between X-ray flux and star clusters. The contour levels are 15, 29, 43, 57, 71 (in arbitrary units). The letter labels in panel *a* correspond to regions categorized by Fabbiano et al. (1997). The other notations are the same as in Figure 4.

Fig. 14.— Comparison of  $\xi(r)$  with (thick lines) and without (thin lines) clusters from the eastern star formation region. The solid lines represent the B1 sample, while the dot-dashed lines represent the B2 sample. The dashed line represents  $\xi(r)$  for the R clusters (unchanged since there are few R clusters in this region). Note that the rank ordering of  $\xi(r)$  for the R, B1, and B2 clusters is not altered by the removal of the eastern star formation region.

Fig. 15.— Association between the HI line-of-sight velocity and star clusters. The HI velocity contour levels are equally spaced starting at  $1450 \text{ km s}^{-1}$ , with an interval of  $15 \text{ km s}^{-1}$ . A gray-scale image is overlaid in panel *a* to show the relative line-of-sight velocities, with darker shades representing higher velocities. Panel *d* shows the cross-correlation functions between the clusters and the velocity gradients. The red object WS#80 is marked in panel *a*, while knots B, E, and F are labeled in panel *b*. The three sets of vertical lines at  $r \approx 1'', 10'', 20''$  show the uncertainties in  $\xi(r)$ . The other notations are the same as in Figure 4.

Fig. 16.— Association between HI velocity dispersion and star clusters. The HI velocity dispersion contour levels are equally spaced, starting at  $5 \text{ km s}^{-1}$ , with an interval of  $5 \text{ km s}^{-1}$ . The numbers show the average velocity dispersions in  $\text{km s}^{-1}$  within their corresponding regions. A gray-scale image is overlaid in panel *a* to show the relative line-of-sight velocities, with darker shades representing higher velocities. Panel *d* shows the cross-correlation functions between the clusters and the velocity gradients. The three sets of vertical lines at  $r \approx 1'', 10'', 20''$  show the uncertainties in  $\xi(r)$ . The other notations are the same as in Figure 4.

Fig. 17.— Association between the  $\text{H}\alpha$  line-of-sight velocity and star clusters. The notations are the same as in Figure 15.

Fig. 18.— Star formation rate ( $\Sigma_{\text{SFR}}$ ) versus gas density ( $\Sigma_{\text{gas}}$ ) in different regions of the Antennae galaxies. The open circles are for atomic gas only, while the filled circles are for the sum of atomic and molecular gas.  $\Sigma_{\text{SFR}}$  is converted from  $\text{H}\alpha$  flux using a coefficient of  $7.9 \times 10^{42}$  (Kennicutt 1998), and an extinction of 1.8 magnitudes in the  $\text{H}\alpha$  flux (see text). The dashed lines are the fits to the total gas density (filled circles). The solid lines represent the Schmidt law  $\Sigma_{\text{SFR}} = (2.5 \pm 0.7) \times 10^{-4} \Sigma_{\text{gas}}^{1.4 \pm 0.15}$  (Kennicutt 1998). Panel *a* shows the relation with a grid resolution of  $11.4'' \times 11.4''$ , panel *b* with  $28.5'' \times 28.5''$ .

Fig. 19.— Cluster formation rate ( $\Sigma_{\text{CFR}}$ ) versus gas density ( $\Sigma_{\text{gas}}$ ) in different regions of the Antennae galaxies. The open circles are for atomic gas only, while the filled circles are for the sum of atomic and molecular gas.  $\Sigma_{\text{CFR}}$  is defined as the density of the R and B1 clusters divided by the average age of 8 Myr. The dashed lines are the fits to the total gas density (filled circles). The solid lines represent the relation  $\Sigma_{\text{CFR}} \propto \Sigma_{\text{gas}}^{1.4}$ . Panel *a* shows the relation with a grid resolution of  $11.4'' \times 11.4''$ , panel *b* with  $28.5'' \times 28.5''$ .

Table 1. Red Clusters

Number	$\Delta$ R.A. <sup>a</sup>	$\Delta$ Decl. <sup>a</sup>	Chip	$M_V$	$B - V$	$V - I$	$\Delta V_{1-6}$ <sup>b</sup>	WS95 Number <sup>c</sup>
1	-7.71	-7.14	2	-8.32	1.47	2.25	1.92	356
2	32.28	-38.13	3	-8.14	1.96	3.00	1.86	124
3	28.87	-56.58	3	-7.89	1.99	2.92	2.08	80
4	31.17	-7.63	3	-7.63	–	2.85	2.08	355
5	28.56	-45.48	3	-7.55	2.51	2.81	2.22	
6	32.82	-36.44	3	-7.51	1.94	2.58	1.64	132
7	28.74	-45.20	3	-7.48	1.71	2.22	3.25	
8	30.33	-30.30	3	-7.24	1.88	2.16	2.75	
9	23.20	-38.08	3	-7.18	2.22	3.25	2.21	125
10	5.46	39.93	2	-7.16	2.71	2.04	1.67	
11	31.00	-7.63	3	-7.05	2.53	3.10	3.10	355
12	26.48	-26.38	3	-6.97	1.63	2.32	2.06	
13	36.03	-33.44	3	-6.96	2.16	2.90	1.77	
14	28.44	-49.18	3	-6.93	2.07	2.19	2.56	
15	21.01	-47.91	3	-6.88	0.50	2.04	1.84	
16	3.96	33.05	2	-6.85	1.84	2.36	1.67	
17	-23.42	17.24	2	-6.77	1.97	2.07	2.57	
18	-0.64	2.57	2	-6.76	–	2.33	1.92	
19	32.91	-30.09	3	-6.75	2.79	2.04	2.86	
20	-2.08	11.24	2	-6.72	0.97	2.24	1.77	
21	2.36	33.25	2	-6.72	0.96	2.06	2.25	
22	-8.17	-16.34	3	-6.66	1.55	2.07	2.59	
23	-19.31	-17.68	1	-6.65	1.39	2.22	2.73	
24	26.27	-24.23	3	-6.65	2.70	2.19	2.69	
25	24.45	-49.07	3	-6.63	0.82	2.11	2.32	
26	-9.64	33.61	2	-6.62	1.49	2.12	2.43	
27	-27.91	0.72	1	-6.61	1.64	2.12	2.78	
28	17.58	-60.77	3	-6.60	–	2.08	1.69	
29	12.10	-3.24	3	-6.59	2.07	2.13	2.89	
30	1.45	25.40	2	-6.56	–	2.12	1.40	
31	12.17	-3.21	3	-6.56	1.27	2.06	2.66	
32	-30.38	-6.92	1	-6.54	1.58	2.14	1.61	
33	-11.19	16.84	2	-6.54	–	2.31	2.00	
34	26.08	-29.41	3	-6.52	2.29	2.14	2.10	
35	40.39	-7.66	3	-6.44	–	2.36	2.57	
36	9.34	33.45	2	-6.43	1.77	2.05	1.32	
37	-27.99	0.85	1	-6.41	0.85	2.20	2.61	
38	-2.65	28.67	2	-6.37	1.62	2.08	1.67	

Table 1—Continued

Number	$\Delta$ R.A. <sup>a</sup>	$\Delta$ Decl. <sup>a</sup>	Chip	$M_V$	$B - V$	$V - I$	$\Delta V_{1-6}$ <sup>b</sup>	WS95 Number <sup>c</sup>
39	32.00	-38.04	3	-6.37	0.67	2.79	2.95	124
40	31.72	-1.77	3	-6.36	—	2.39	2.35	
41	-19.90	-25.76	4	-6.29	—	2.01	1.81	
42	-27.63	0.64	1	-6.29	1.35	2.20	2.38	
43	67.95	-19.34	3	-6.28	0.70	2.17	2.56	
44	31.73	-11.11	3	-6.27	2.18	2.74	1.83	
45	66.37	-20.12	3	-6.24	2.02	2.13	2.86	
46	-39.36	-1.37	1	-6.23	—	2.20	1.88	
47	33.55	-22.04	3	-6.22	—	2.19	2.53	
48	-31.59	-5.02	1	-6.22	1.04	2.06	2.30	
49	37.27	-32.52	3	-6.20	1.19	2.37	0.37	
50	26.84	-16.52	3	-6.14	1.47	2.34	2.40	
51	24.15	-22.99	3	-6.11	2.06	2.09	2.01	
52	32.65	-4.88	3	-6.11	2.81	2.03	0.61	
53	23.22	-2.54	3	-6.08	2.44	2.37	1.33	
54	4.22	-59.14	4	-6.08	1.18	2.42	1.13	
55	39.66	-49.98	3	-6.06	2.67	2.31	2.15	
56	48.78	15.74	3	-6.02	2.26	2.17	1.63	
57	-20.04	-14.99	1	-6.00	—	2.66	1.81	
58	28.26	-42.08	3	-6.00	1.65	2.26	2.17	
59	6.12	22.69	2	-5.98	—	2.09	1.53	
60	-25.74	-18.11	1	-5.94	—	2.11	1.79	
61	42.69	-56.09	3	-5.92	—	2.47	1.17	
62	29.25	-8.45	3	-5.85	1.57	2.20	1.93	
63	34.00	-44.39	3	-5.84	1.29	2.27	1.91	
64	-33.70	-15.47	1	-5.82	—	2.58	1.28	
65	46.27	-44.23	3	-5.82	—	2.23	1.98	
66	40.07	-21.60	3	-5.78	—	2.38	1.55	
67	26.03	-24.79	3	-5.76	2.17	2.59	1.81	
68	18.73	-0.58	3	-5.73	—	3.32	2.50	
69	-30.50	-15.71	1	-5.73	2.33	2.30	1.62	
70	31.70	-29.35	3	-5.67	1.38	2.71	1.96	
71	-42.57	1.88	1	-5.64	0.89	2.36	2.43	
72	-41.09	-2.09	1	-5.55	—	2.60	2.23	
73	36.10	-21.07	3	-5.39	—	2.95	1.52	
74	25.61	-42.25	3	-5.39	1.04	2.54	1.78	
75	45.50	-33.12	3	-5.30	0.69	2.42	1.03	
76	-29.78	3.48	1	-5.24	—	2.58	2.25	

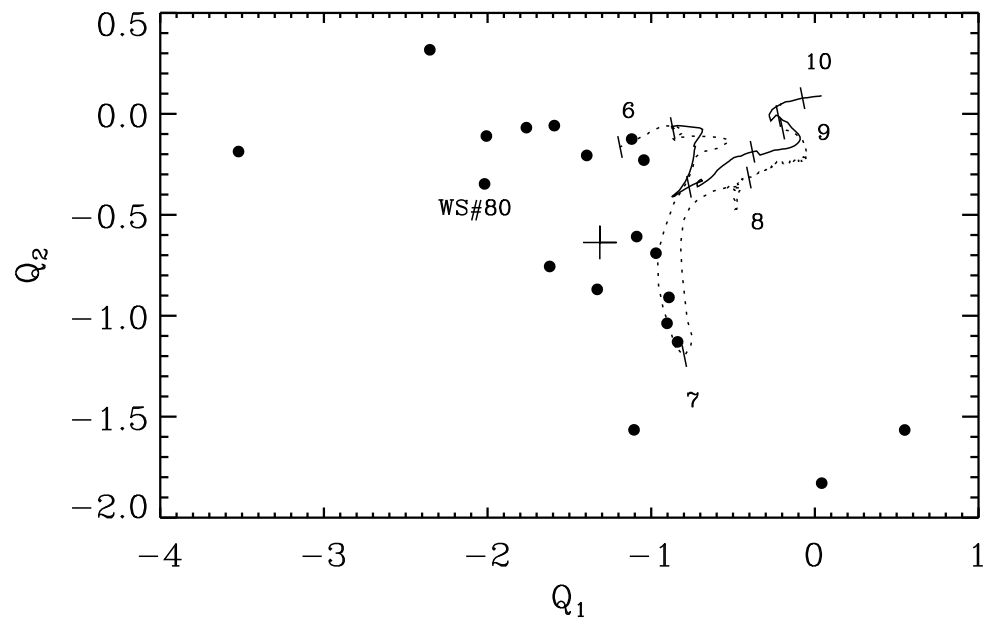
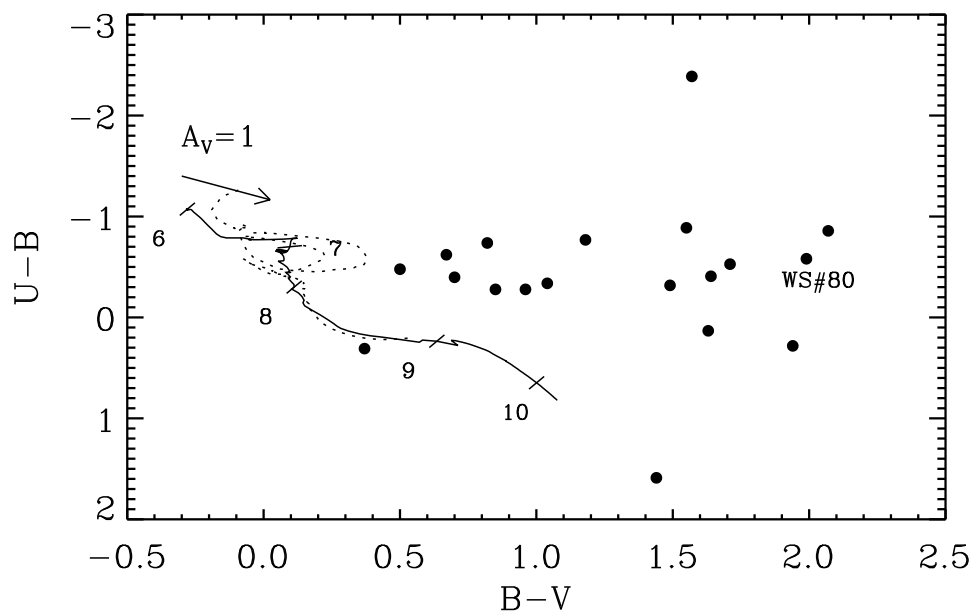
Table 1—Continued

Number	$\Delta$ R.A. <sup>a</sup>	$\Delta$ Decl. <sup>a</sup>	Chip	$M_V$	$B - V$	$V - I$	$\Delta V_{1-6}$ <sup>b</sup>	WS95 Number <sup>c</sup>
77	26.15	-28.16	3	-5.18	1.29	3.15	1.10	
78	-48.24	-11.58	1	-5.12	–	2.72	1.57	
79	30.40	-44.14	3	-4.94	–	2.86	1.11	
80	24.94	-42.67	3	-4.88	1.04	4.12	1.76	
81	15.90	-32.21	3	-4.83	1.25	2.71	0.35	
82	-20.49	-21.53	4	-4.82	–	2.81	1.91	
83	22.95	-49.74	3	-4.69	–	2.97	0.19	
84	-41.36	-4.80	1	-4.37	–	3.04	0.05	

<sup>a</sup>Following the convention used in Whitmore & Schweizer (1995) and Whitmore et al. (1999), the coordinates are the offsets in arcseconds from R.A. =  $12^h 01^m 52.97^s$  and Decl. =  $-18^\circ 52' 08.29''$  (J2000.0), near the center of NGC 4038.

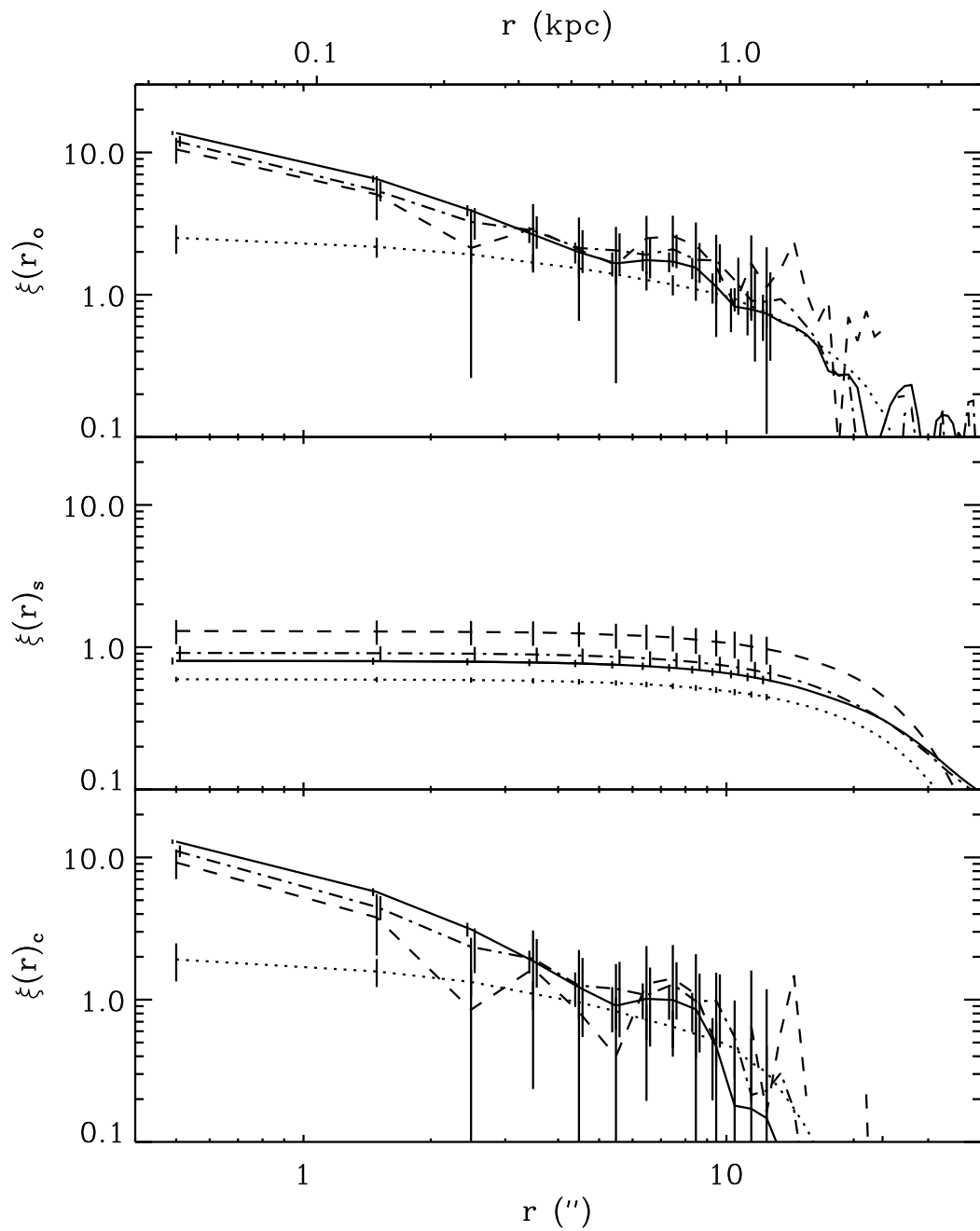
<sup>b</sup>Objects with  $\Delta V_{1-6} < 1.0$  are likely to be cosmic rays.

<sup>c</sup>Number assigned by Whitmore & Schweizer (1995). Duplicated numbers are neighboring objects, generally because of differences in spatial resolution between the cycle 2 and cycle 5 observations.



This figure "fig2.jpg" is available in "jpg" format from:

<http://arxiv.org/ps/astro-ph/0105174v2>

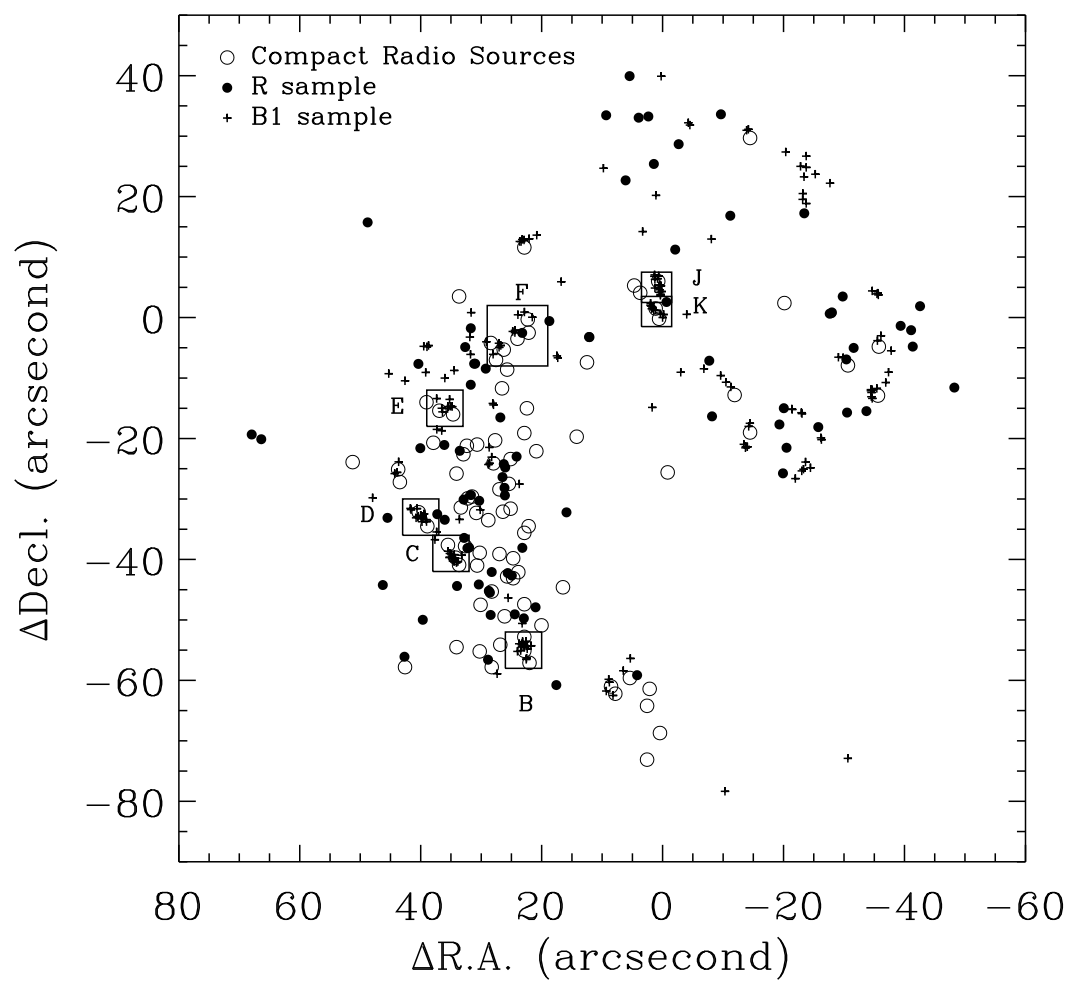


This figure "fig4.jpg" is available in "jpg" format from:

<http://arxiv.org/ps/astro-ph/0105174v2>

This figure "fig5.jpg" is available in "jpg" format from:

<http://arxiv.org/ps/astro-ph/0105174v2>



This figure "fig7.jpg" is available in "jpg" format from:

<http://arxiv.org/ps/astro-ph/0105174v2>

This figure "fig8.jpg" is available in "jpg" format from:

<http://arxiv.org/ps/astro-ph/0105174v2>

This figure "fig9.jpg" is available in "jpg" format from:

<http://arxiv.org/ps/astro-ph/0105174v2>

This figure "fig10.jpg" is available in "jpg" format from:

<http://arxiv.org/ps/astro-ph/0105174v2>

This figure "fig11.jpg" is available in "jpg" format from:

<http://arxiv.org/ps/astro-ph/0105174v2>

This figure "fig12.jpg" is available in "jpg" format from:

<http://arxiv.org/ps/astro-ph/0105174v2>

This figure "fig13.jpg" is available in "jpg" format from:

<http://arxiv.org/ps/astro-ph/0105174v2>

This figure "fig14.jpg" is available in "jpg" format from:

<http://arxiv.org/ps/astro-ph/0105174v2>

This figure "fig15.jpg" is available in "jpg" format from:

<http://arxiv.org/ps/astro-ph/0105174v2>

This figure "fig16.jpg" is available in "jpg" format from:

<http://arxiv.org/ps/astro-ph/0105174v2>

This figure "fig17.jpg" is available in "jpg" format from:

<http://arxiv.org/ps/astro-ph/0105174v2>

